European Journal of Pharmaceutical Sciences 221 (2026) 107519

Contents lists available at ScienceDirect

European Journal of Pharmaceutical Sciences

journal homepage: www.elsevier.com/locate/ejps

Sustainable chemistry and preclinical characterization of RC-106·HCl: A brain-penetrant pan sigma receptor modulator for glioblastoma

Noemi Marino [a,1], Roberta Listro [b,1], Chiara Milanese [c], Martina Bedeschi [a], Elena Cavassi [a], Carolina Palazzi [a], Marco Cambiaghi [d,e], Mario Rosario Buffelli [d], Fabio Nicolini [f], Giulio Massimo Dondio [g], Giacomo Rossino [b], Pasquale Linciano [b], Daniela Rossi [b], Simona Collina [b], Anna Tesei [a,*]

[a] Biosciences Laboratory, IRCCS Istituto Romagnolo per lo Studio dei Tumori (IRST) "Dino Amadori", 47014 Meldola, Italy
[b] Department of Drug Sciences, University of Pavia, Via Taramelli 12, 27100 Pavia, Italy
[c] Department of Chemistry, University of Pavia, Via Taramelli 12, 27100 Pavia, Italy
[d] Department of Neurosciences, Biomedicine and Movement Sciences, University of Verona, 37124 Verona, Italy
[e] Department of Neurology, Hackensack Meridian School of Medicine, Nutley, NJ 07110, USA
[f] Advanced Cellular Therapies and Rare Tumors Unit, IRCCS IRST "Dino Amadori", Meldola, Italy
[g] Aphad Srl, Via della Resistenza 65, 20090 Buccinasco, Italy

ARTICLE INFO

Keywords:
Sigma receptors
Glioblastoma
Sustainable synthesis
2D and 3D cell cultures
PDOX
In vivo experiments

ABSTRACT

RC-106 is a Sigma receptor modulator under investigation as a potential therapeutic agent for glioblastoma (GBM). Here, we report a multigram-scale synthesis based on green chemistry principles, its comprehensive solid-state characterization, and its preclinical evaluation *in vitro* and *in vivo*. ADMET prediction indicated good drug-likeness, absence of PAINS features, compliance with Lipinski criteria, favorable metabolic stability, and the ability to cross the blood–brain barrier. The optimized synthetic process to obtain **RC-106**·HCl (>99% purity) for solid-state characterization performed by TGA, DSC, FT-IR, XRPD, and SEM, confirming the compound crystalline nature and appropriate thermal behavior. *in vivo*, **RC-106** consistently reduced cell viability in both commercial (U87, A172) and patient-derived GBM cell lines (G34, G48) under hypoxic conditions, inducing apoptosis and neurosphere disaggregation with IC_{50} values between 44 and 54 μM. *In vivo*, using a patient-derived orthotopic xenograft (PDOX) mouse model, daily administration of **RC-106**·HCl (20 mg/kg) was well tolerated, with no observable systemic or neurological toxicity, as evidenced by stable body weight and preserved motor performance. Intraperitoneal administration of **RC-106**·HCl, although it did not definitively arrest tumor growth, resulted in a time-dependent reduction in intracranial GBM burden in our patient-derived orthotopic xenograft (PDOX) model. Pharmacokinetic and biodistribution analyses supported rapid absorption and distribution to the brain and spinal cord. Overall, **RC-106**·HCl shows promising *in vitro* anti-GBM activity and an excellent safety profile *in vivo*, while further optimization is needed to enhance its pharmacokinetic properties and therapeutic effectiveness.

1. Introduction

Glioblastoma (GBM), IDH-wild type (Louis et al., 2021), is the most aggressive primary brain tumor in adults.(Schaff and Mellinghoff, 2023) The current standard of care, adopted approximately 20 years ago, consists of maximal safe surgical resection followed by radiotherapy and temozolomide chemotherapy.(Stupp et al., 2005) Despite this multimodal and aggressive approach, the highly invasive nature of the tumor, its localization within the brain parenchyma, and the relentless development of therapy resistance inevitably lead to disease progression and a fatal outcome in virtually all patients, with a 5-year survival rate that remains as low as 6.6% (Weller et al., 2021).

The current GBM treatment landscape is still dominated by only three FDA-approved agents (Fig. 1): carmustine (BiCNU), temozolomide

* Corresponding author.
E-mail addresses: simona.collina@unipv.it (S. Collina), anna.tesei@irst.emr.it (A. Tesei).
[1] These authors contributed equally to this work.

https://doi.org/10.1016/j.ejps.2026.107519
Received 23 January 2026; Received in revised form 25 March 2026; Accepted 28 March 2026
Available online 29 March 2026

(Temodar), and Bevacizumab (Avastin), which provide limited survival benefit and are associated with resistance and toxicity (Nabors et al., 2020).

While these drugs modestly extend median survival, the overall prognosis remains dismal. No effective standard of care exists for recurrent GBM, highlighting the critical unmet medical need for innovative therapeutic approaches. This urgent need and limited armamentarium of approved drugs have driven intense pharmaceutical development activity.

An analysis supported by IQVIA highlights a robust pipeline of investigational compounds, with seventy-eight chemical entities at various stages of development, ranging from early discovery to late-stage clinical trials (IQVIA, 2025). In detail, one agent is in early stage of discovery, twelve are in preclinical studies, twenty-four in Phase I, thirty-one in Phase II, nine in Phase III, and one drug is submitted for approval (Fig. 2). Major pharmaceutical companies and biotechnology firms, including Bayer, Chimerix, Aivita Biomedical, Denovo Biopharma, Northwest Therapeutics, and VBL Therapeutics, among others, are actively advancing candidates through clinical trials. Specifically, the preclinical pipeline includes several novel molecules (e.g., TUG1 ASO (Katsushima et al., 2016), INV441 (invIOs, 2025), NPT520–337 (Fonkem et al., 2022), Brincidofovir (Seo et al., 2025), BEN-28,010 (Rawling et al., 2025), MB-109 (Mustang Bio, Inc., 2025), NMS-173 (Magnaghi et al., 2022), RBD8088 (Grönros et al., 2024)), developed across the USA, Japan and Europe. These candidates target various mechanisms of action with projected launch timelines extending into the next decade. However, the concentration of compounds in Phase II, with limited progression to Phase III, reflects the significant attrition risk inherent in GBM drug development, largely due to the complex tumor biology, drug-delivery challenges related to the blood–brain barrier, the poor reproducibility of positive Phase II results in subsequent Phase III trials, and patient-accrual difficulties (Di Nunno et al., 2021; Hotchkiss et al., 2024; Mandel et al., 2018; Sarkaria et al., 2018; Shah et al., 2022; Vanderbeek et al., 2018).

In line with these efforts from both academia and industry, our research group has focused on the discovery of new molecular entities endowed with high therapeutic potential and good efficacy against GBM cell lines.

Several biological and clinical challenges underlie this therapeutic issue to this unmet need. The blood–brain barrier (BBB) severely limits drug delivery, and although GBM is associated with regions of increased vascular permeability, malignant cells often remain protected within intact BBB areas (Noorani and de la Rosa, 2023). Additionally, pronounced intratumoral heterogeneity drives therapeutic resistance, contributing to treatment failure and limiting survival outcomes. These facts underscore that, despite an apparently crowded pipeline (Fig. 2), very few candidates successfully progress to approval, mainly because of

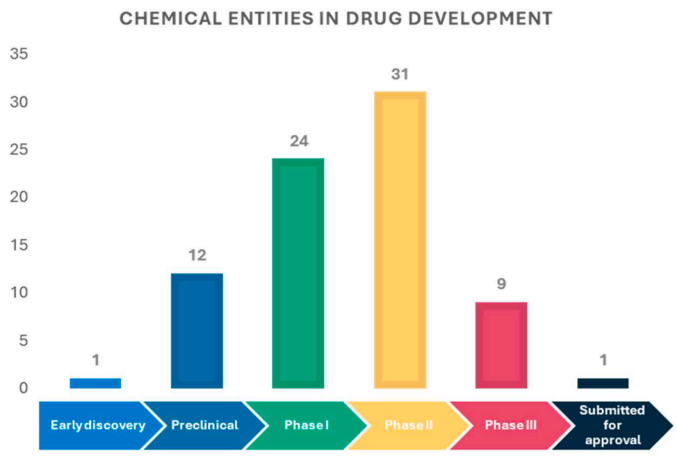

Fig. 2. Number of compounds under investigation for the treatment of GBM, divided by their current stage of drug discovery and development (source: IQVIA) (IQVIA, 2025).

the complex biology of GBM and delivery barriers. In this context, our in-house developed compound **RC-106** is positioned in the preclinical segment of this pipeline as a Sigma receptor modulator with documented pro-apoptotic activity in GBM models and brain penetration, and thus represents a mechanistically distinct approach within the current landscape.

Sigma receptors, consisting of Sigma-1 (S1R) and Sigma-2 (S2R) receptor subtypes, represent promising targets that may address some of these challenges in GBM biology (Collina et al., 2017). S1R acts as a protein chaperone and is overexpressed in GBM, where it regulates cell proliferation and survival pathways (Wang et al., 2025). Similarly, S2R is overexpressed in GBM and is associated with poor prognosis and increased malignancy (Liu et al., 2019; Wheeler et al., 2000). Targeting these receptors with specific modulators offers a novel therapeutic approach that could potentially overcome traditional resistance mechanisms. Although several classes of Sigma receptor ligands with antiproliferative activity are under investigation, including mixed S1R and S2R modulators that act as pan-Sigma agents in oncology settings, they have not yet reached regulatory approval and are not currently in clinical trials (Fallica et al., 2021; Georgiadis et al., 2017; Oyer et al., 2019).

Within this context, **RC-106**·HCl was identified by us as a pan-Sigma receptor modulator, with a unique dual profile: S1R antagonist and S2R agonist activity (K_i S1R= 12 nM; K_i S2R= 22 nM) (Fig. 3) (Listro et al., 2020; Rui et al., 2016). Preliminary studies demonstrated broad anticancer efficacy towards multiple tumor cell lines, including GBM,

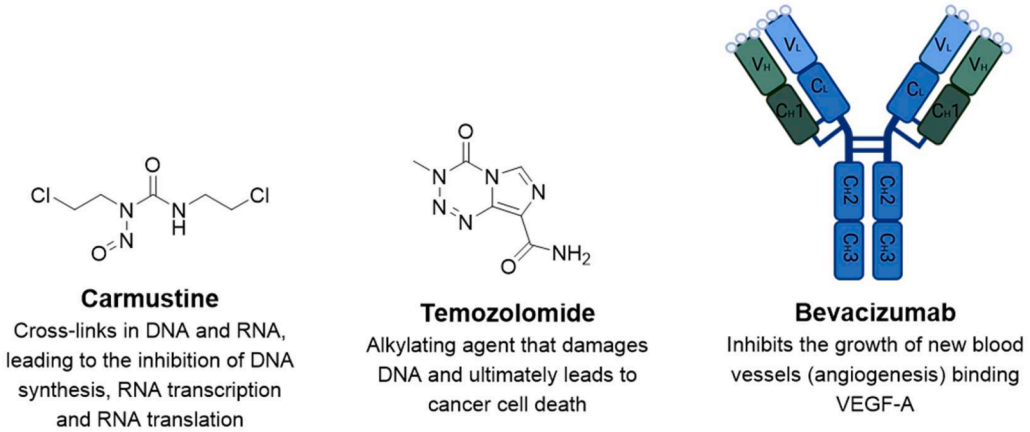

Fig. 1. Structures and mechanisms of action of the three approved drugs against GBM.

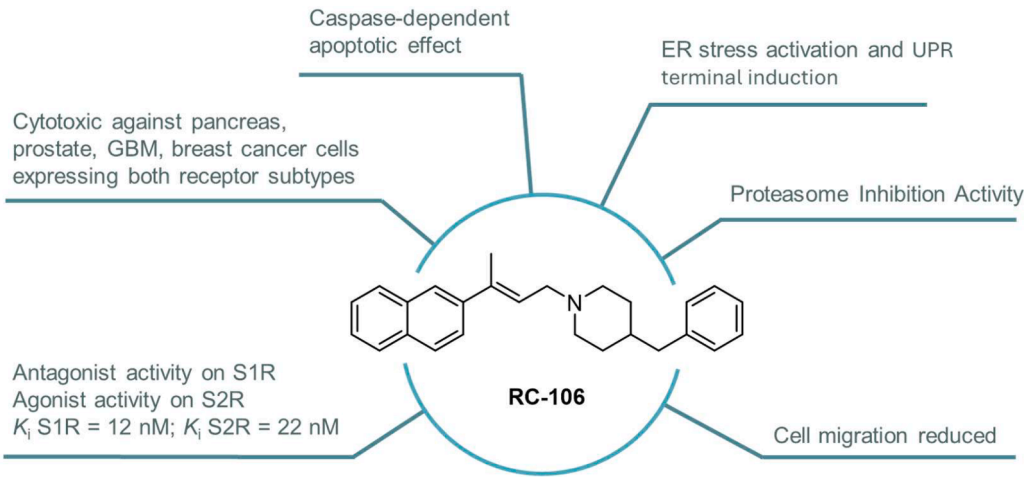

Fig. 3. Chemical structure and biological profile of RC-106.

prostate, breast, and pancreatic cancers. **RC-106** induces significant cytotoxicity through caspase-dependent apoptosis, and modulates endoplasmic reticulum stress and the unfolded protein response (ER-UPR), that are pathways commonly dysregulated in aggressive malignancies (Tesei et al., 2018). As a result, **RC-106** reduces cell viability, enhances apoptotic signaling, and inhibits tumor cell motility. The correlation between the effects of **RC-106** and the modulation of Sigma receptors was confirmed by functional studies incorporating S1R and S2R gene silencing approaches (Cortesi et al., 2020).

These findings suggested **RC-106** as a potential candidate to counteract GBM progression through a Sigma receptor modulation mechanism.

Building on these encouraging results and recognizing that Sigma receptors may represent an innovative and more effective target for GBM, we report the multigram-scale synthesis of **RC-106**, based on green chemistry principles, its comprehensive solid-state characterization, and preclinical evaluation to assess its therapeutic potential and identify translational barriers.

To achieve this, we first evaluated in silico the ability of **RC-106** to cross the blood–brain barrier (BBB), a major bottleneck in the drug discovery pipeline for CNS diseases. We then conducted an extensive assessment of its activity using *in vitro* GBM models, integrating conventional two-dimensional (2D) cultures (including both commercial and patient-derived cell lines) with three-dimensional (3D) neurosphere systems. Following confirmation of *in vitro* efficacy, pharmacokinetic and biodistribution, studies *in vivo* were performed to verify the ability of **RC-106** to reach the target brain tissue. Lastly, we evaluated tolerability and preliminary efficacy using a patient-derived orthotopic xenograft (PDOX) mouse model of GBM.

This integrated approach provides a thorough characterization of physicochemical properties, brain penetration, pharmacological activity, and safety profile of **RC-106**, while identifying key translational challenges that require optimization in future development.

2. Materials and methods

2.1. Chemistry

2.1.1. General information

All reagents and solvents used for synthesis were purchased from Sigma-Aldrich (Italy), VWR or Fluorochem and used without further purification. Thin-layer chromatography (TLC) was performed on silica gel precoated aluminium-plates (Fluka Kieselgel 60 F254, Merck). Visualization of TLC spots was achieved under UV light or by applying alcoholic ninhydrin, cerium ammonium molybdate (IV), or alkaline potassium permanganate solutions. Büchi Pure C-810 Flash system was used for automated chromatography, using SiliaSep Flash Cartridges (SiliCycle). Dried, untreated Celite® S (CAS 61,790-53–2) was used for filtration.

Nuclear Magnetic Resonance (NMR) spectra were recorded at 25 °C using Bruker Avance 400 spectrometer with 1H at 400.134 MHz and 13C at 100.62 MHz instrument. Proton chemical shifts (δ) are expressed in parts per million (ppm) and referenced to residual solvent peak ($CDCl_3$: δ = 7.26 ppm. Signal multiplicities are reported as follows: s (singlet), d (doublet), t (triplet), q (quartet), m (multiplet), and br (broad). Coupling constants (*J*) are given in Hertz (Hz). ^{13}C NMR spectra were recorded under complete proton decoupling conditions, with chemical shifts referenced to residual solvent peak ($CDCl_3$: δ = 77.23 ppm).

Compound purity was assessed by HPLC-UV/PDA analysis using a Jasco system (Tokyo, Japan) equipped with a PU-1580 pump and a MD-1510 photodiode array (PDA) detector. Data acquisition and processing were carried out using ChromNAV software (Jasco, Tokyo, Japan). Chromatographic separations were carried out on XBridge Phenyl column (5 μm particle size) at room temperature. The chromatographic method employed a flow rate of 1 mL/min, with an injection volume of 10 μL. Detection was carried out at a wavelength of 254 nm. The mobile phases consisted of solvent A: water with 0.1% formic acid, and solvent B: acetonitrile with 0.1% formic acid. The following gradient program was applied: starting at 90% A and 10% B, linearly changing to 10% A and 90% B over 10 min, held constant until minute 12, followed by re-equilibration to initial conditions (90% A, 10% B) at minute 13, and maintained until minute 18. The final compounds exhibited purity >99%.

2.1.2. Synthesis of (E)-ethyl 3-(naphthalen-2-yl) but-2-enoate (*1*)

In a 2-necked 2 L round-bottom flask, previously dried in an oven at 100 °C overnight and flushed with nitrogen, 2-bromonaphthalene (20.70 g, 0.1 mol, 1.0 equiv), TEAC (51.86 g, 0.313 mol, 3.1 equiv), sodium acetate (20.75 g, 0.253 mol, 2.5 equiv), and PdEnCat® (2.07 g, 0.4 mmol/g, 0.008 equiv) were added. The mixture was suspended in ethanol (265 mL), followed by addition of ethyl crotonate (10.48 mL, 0.1 mol, 1.0 equiv). The reaction mixture was stirred overnight at room temperature.

After completion, the reaction was vacuum filtered to recover the catalyst, and the filtrate was concentrated under reduced pressure. The crude residue was dissolved in ethyl acetate (300 mL) and washed three times with water. The aqueous phase was extracted with AcOEt to recover any remaining product. The combined organic layers were dried over Na_2SO_4, filtered, and concentrated under reduced pressure to afford 26 g of crude product.

The crude material was subjected to precipitation in Heptane (170

mL, overnight). The resulting solid was collected by vacuum filtration, yielding 23.6 g of crude product, which was then passed through a short silica gel plug and further purified by flash chromatography using a Büchi Pure C-810 system. This afforded 10.85 g of pure E-isomer as a colorless solid in 45% yield. Rf = 0.5 (Hexane/Ethyl acetate, 95:5 v/v).

^{1}H NMR (400 MHz, $CDCl_3$) δ: 7.86 (s, 1H, aromatic), 7.80–7.70 (m, 3H), 7.51 (d, J = 8.6 Hz, 1H), 7.44–7.37 (m, 2H), 6.20 (s, 1H), 4.16 (q, J = 7.1 Hz, 2H), 2.60 (s, 3H), 1.25 (t, J = 7.1 Hz, 3H).

^{13}C NMR (101 MHz, $CDCl_3$) δ: 165.9, 154.2, 138.3, 132.4, 132.1, 127.5, 127.1, 126.5, 125.6, 125.4, 124.9, 122.9, 116.5, 58.9, 16.9, 13.3.

2.1.3. Synthesis of (E)-3-(naphthalen-2-yl)but-2-enoic acid (2)

Compound **1** (10.85 g, 45.15 mmol, 1.0 equiv) was dissolved in a mixture of ethanol/THF (3:1, 215 mL) together with 3 M NaOH aqueous solution (15 mL, 0.4515 mol, 10 equiv) in a 1 L round-bottom flask. The reaction mixture was stirred overnight at room temperature, after which the solvents were removed under reduced pressure.

The resulting residue was dissolved in DCM and extracted with 1 M aqueous HCl solution (3 × 400 mL). The aqueous phase was extracted with DCM. The combined organic layers were dried over Na_2SO_4, filtered, and evaporated under reduced pressure to give 12.05 g of crude product.

Purification was performed by crystallization using an acetone/water mixture (6:4 v/v), affording 5.71 g of pure product as a colorless solid in 60% yield. Rf = 0.22 (Hexane/Ethyl acetate 9:1 + 1% formic acid, v/v/v).

^{1}H NMR (400 MHz, DMSO) δ: 12.29 (brs, 1H), 8.14 (d, J = 1.6 Hz, 1H), 8.02–7.98 (m, 1H), 7.95–7.92 (m, 2H), 7.73 (dd, J = 2.0, 8.7 Hz, 1H), 7.58–7.54 (m, 2H), 6.29 (q, J = 1.2 Hz, 1H), 2.62 (d, J = 1.2 Hz, 3H).

^{13}C NMR (101 MHz, DMSO) δ: 168.1, 153.7, 139.1, 133.5, 133.3, 129.0, 128.5, 127.9, 127.3, 127.0, 126.3, 124.4, 118.5, 17.6.

2.1.4. Synthesis of (E)-1-(4-benzylpiperidin-1-yl)-3-(naphthalen-2-yl) but-2-en-1-one (3)

In a 500 mL round-bottom flask, previously dried and flushed with nitrogen, compound **2** (5.65 g, 26.6 mmol, 1.0 equiv), 4-benzylpiperidine (5.6 g, 31.9 mmol, 1.2 equiv), TBTU (10.24 g, 31.9 mmol, 1.2 equiv), and TEA (8.81 mL, 63.8 mmol, 2.4 equiv) were dissolved in DMF (200 mL). The mixture was stirred in an ice bath for 30 min, then allowed to warm to room temperature and stirred overnight under a nitrogen atmosphere.

Reaction progress was monitored by TLC (mobile phase: hexane/ethyl acetate 1:1 + 1% formic acid, v/v/v) until completion. The white precipitate formed was filtered using a sintered glass funnel, and the filtrate was concentrated under reduced pressure. The crude residue was dissolved in ethyl acetate and subjected to sequential liquid-liquid extraction with 1 M HCl (× 3), saturated $NaHCO_3$ (× 3), and brine (× 3). The organic phase was dried with Na_2SO_4, filtered, and concentrated. The extraction allows to obtain 9.12 g of the target compound as white solid in 93% yield. Rf = 0.57 (Hexane/Ethyl acetate 1:1 + 1% formic acid, v/v/v)

^{1}H NMR (400 MHz, $CDCl_3$) δ: 7.83–7.71 (m, 4H), 7.52 (dd, J = 8.6, 1.9 Hz, 1H), 7.43–7.37 (m, 2H), 7.24–7.18 (m, 2H), 7.15–7.04 (m, 3H), 6.34 (q, J = 0.9 Hz, 1H), 4.62 (d, J = 13.2 Hz, 1H), 3.92 (d, J = 13.5 Hz, 1H), 2.98–2.85 (m, 1H), 2.57 (dd, J = 12.8, 2.4 Hz, 1H), 2.49 (dd, J = 12.4, 6.2 Hz, 2H), 2.27 (d, J = 1.0 Hz, 3H), 1.77–1.59 (m, 3H), 1.22–1.04 (m, 2H).

^{13}C NMR (101 MHz, $CDCl_3$) δ: 167.1, 143.9, 140.0, 138.7, 133.3, 133.1, 129.1, 128.3, 128.3, 128.0, 127.6, 126.4, 126.3, 126.1, 125.1, 123.9, 120.8, 46.8, 43.0, 41.7, 38.4, 32.8, 31.9, 17.9.

2.1.5. Synthesis of (E)-4-benzyl-1-(3-(naphthalen-2-yl)but-2-en-1-yl) piperidine (RC-106)

In a 500 mL two-neck round-bottom flask, previously dried and flushed with nitrogen, compound **3** (9.12 g, 24.7 mmol, 1.0 equiv) was dissolved in anhydrous DCM (85 mL). TMSCl (3.75 mL, 29.6 mmol, 1.2 equiv) was added, and after 10 min, $LiAlH_4$ (37.02 mL, 37.0 mmol, 1.5 equiv) was added dropwise *via* a dropping funnel. The reaction mixture was stirred for 40 min at room temperature and monitored by TLC (hexane/ethyl acetate 6:4, v/v). After completion, the reaction was quenched sequentially with ethyl acetate, methanol, and water until gas evolution ceased and lithium salts precipitated. The mixture was filtered through Celite, washing with DCM. After every three DCM washes, one water wash was performed. This washing cycle was repeated until full product recovery.

H_2O/DCM mixture was concentrated under reduced pressure, the phases were separated in a separatory funnel, and the aqueous phase was extracted with DCM (3 × 50 mL). The combined organic layers were dried over Na_2SO_4 and evaporated under reduced pressure, affording 7.56 g of crude product. Purification was performed by crystallization with hot ethanol, affording 5.66 g of pure product as pale-yellow solid (65% yield). Rf = 0.45 (hexane/ethyl acetate 6:4, v/v).

^{1}H NMR (400 MHz, $CDCl_3$) δ: 7.86–7.69 (m, 4H), 7.52 (dt, J = 11.2, 5.6 Hz, 1H), 7.40–7.31 (m, 2H), 7.24–7.19 (m, 2H), 7.15–7.05 (m, 3H), 6.00 (t, J = 6.7 Hz, 1H), 3.13 (d, J = 6.7 Hz, 2H), 2.94 (d, J = 11.7 Hz, 4H), 2.48 (d, J = 7.0 Hz, 2H), 2.08 (d, J = 0.7 Hz, 3H), 1.60 (m, 2H), 1.29 (m, 3H).

^{13}C NMR (101 MHz, $CDCl_3$) δ: 140.7, 140.4, 136.9, 133.4, 132.5, 129.1, 128.1, 128.0, 127.6, 127.5, 126.0, 125.7, 125.6, 124.2, 124.1, 57.2, 54.1, 43.2, 37.9, 32.2, 16.1.

2.1.6. Synthesis of (E)-4-benzyl-1-(3-(naphthalen-2-yl)but-2-en-1-yl) piperidine hydrochloride (RC-106·HCl)

In a 2 L round-bottom flask, **RC-106** (5.66 g, 15.9 mmol, 1.0 equiv) was dissolved in 900 mL of diethyl ether. A 1 M solution of HCl in diethyl ether (15.9 mL, 15.9 mmol, 1.0 equiv) was added dropwise, resulting in the formation of a white precipitate. The suspension was stored in a refrigerator overnight to allow complete precipitation. The solid was collected by Büchner filtration, and the supernatant was centrifuged to recover any suspended product. The obtained hydrochloride salt was dried under vacuum in a desiccator until constant weight was reached, yielding 6.1 g of a pale-yellow solid (98% yield). Rf = 0.45 (hexane/ethyl acetate 6:4, v/v). Purity>99% (tr= 13 min, k = 3.3)

^{1}H NMR (400 MHz, $CDCl_3$) δ: 12.40 (brs, 1H), 7.82–7.72 (m, 4H), 7.52 (brs, 1H), 7.42 (m, 2H), 7.22 (m, 2H), 7.13 (t, J = 7.1 Hz, 1H), 7.05 (d, J = 7.2 Hz, 2H), 6.19 (s, 1H), 3.77 (brs, 2H), 3.52 (br s, 2H), 2.63–2.58 (brs, 4H), 2.17 (s, 3H), 2.06 (brs, 2H), 1.80–1.77 (brs, 2H), 1.66 (brs, 1H).

^{13}C NMR (101 MHz, $CDCl_3$) δ: 145.2, 139.2, 138.5, 133.2, 133.1, 129.1, 128.5, 128.4, 128.3, 127.6, 126.5, 126.4, 126.4, 125.2, 124.0, 115.0, 52.7, 42.0, 36.7, 29.1, 17.1.

2.1.7. General procedure for recycling PdEnCat® 40

PdEnCat® 40 was recovered by filtration over a Büchner and washed sequentially with 2-propanol and water to remove any residual impurities. A final wash with ethanol was then performed to recondition the catalyst matrix before reusing. As previously reported by us, the catalyst could be re-used at least once in a gram-scale synthesis without significant loss of activity (Rossino et al., 2024).

2.2. Solid-state analysis

Thermogravimetric analysis (TGA) was performed using a Q5000 instrument (TA Instruments, New Castle, DE, USA). Approximately 3 mg of sample were placed in a platinum crucible and heated from 25 °C to 250 °C at a rate of 5 °C/min under a nitrogen flow of 50 mL/min.

Differential scanning calorimetric (DSC) analyses were carried out on a Sensys DSC instrument (Setaram – Kep Technologies, Caluire - France). About 10 mg of sample were placed in an aluminum crucible, heated from 25 °C to 250 °C, and then cooled back to 25 °C at a rate of 5 °C/min under an argon atmosphere.

FT-IR Spectroscopy was conducted using a Nicolet iS10 spectrometer (Nicolet, Madison, WI, USA) in attenuated total reflection (ATR) mode. Spectra were recorded in the range 4000–550 cm^{-1} with a resolution of 4 cm^{-1}.

X-Ray powder diffraction (XRPD) analysis was carried out using a D2 diffractometer (Bruker, Karlsruhe, Germany). Samples were gently pressed into a thin layer on a zero-background silicon sample holder and scanned over the range of 5° to 50°, with a counting time of 5 seconds per step.

Scanning electron microscopy (SEM) was performed using an Evo-Max 10 microscope (Carl Zeiss, Oberkochen, Germany). Samples were coated with a thin layer of gold and analyzed using a LaB_6 electron source at 20 kV accelerating voltage, with a working distance of 8.5 mm. Images were acquired by collecting secondary electrons.

2.3. In vitro experiments

2.3.1. Cell lines

GBM cell lines U87 and A172 were purchased from ATCC (ATCC, Manassas, VA, USA). The U87 cells were grown in Eagle's Minimum Essential Medium supplemented with 10% Fetal Bovine Serum (FBS) (EuroClone S.p.a, Milan, Italy); A172 cells were grown in Dulbecco's Modified Eagle's Medium (ATCC medium), supplemented with 10% FBS (EuroClone S.p.a, Milan, Italy).

GBM primary cultures (G34 and G48) were isolated in our laboratory from surgical samples of GBM obtained from the Neurosurgery Unit of Bufalini Hospital in Cesena and selected by a pathologist. Primary cultures were maintained in NeuroCult™ for primary neuronal and neural stem cell culture (Stemcell Technologies, Vancouver, Canada) at 37 °C. All cell lines, routinely tested for mycoplasma presence, were maintained under hypoxic conditions (1% O_2), as described in our earlier work (Lazzarini et al., 2023). Despite this reduced oxygen tension, both patient-derived GBM primary cells retain a typical exponential growth profile. In particular, the cancer stem phenotype and metabolic profile of G34, as well as its modulation by oxygen tension, have been thoroughly characterized in prior studies (Arienti et al., 2021).

2.3.2. CellTiter-Glo® luminescent cell viability assay

Cell viability of GBM commercial and primary cells was measured using a luminescent cell viability assay (Promega, Milan, Italy), as previously described (Tesei et al., 2019). Briefly, cells were plated in a 96-well opaque culture plate (BD Falcon, Corning, Somerville, MA, USA), CellTiter-Glo® reagent was added to each well and the luminescence signal was read after 30 min with the GloMax® 96 microplate luminometer (Promega, Milan, Italy).

2.3.3. Morphological and biophysical profiling of GBM 3D spheroids

Spheroid formation. For the generation of GBM spheroids, U-shaped, 384-well ULA plates (PrimeSurface®, 384 U PLATE S-bio, Constantine, MI 49,042, USA.) were seeded with cell suspensions as previously described (Peirsman et al., 2021) with a seeding number of 1000 cells/well in a total volume of 80 µl/well. Cells were seeded in three different replicates by different operators. Each operator used a different cell batch deriving from the same original batch.

Morphometric and biophysical characterization. After 5 days of culture, representative brightfield images were captured using an inverted widefield microscope (Olympus IX51 microscope (Olympus Corporation, Tokyo, Japan), equipped with a Nikon Digital Sight DS-Vi1 camera (CCD vision sensor, square pixels of 4.4 µM side length, 1600 × 1200 pixel resolution, 8-bit grey level) (Nikon Instruments, Spa. Florence, Italy). The biophysical characterization of the samples was performed using the W8 Physical Cytometer (CellDynamics ISRL BO, Italy), which allows the measure of mass density, size, weight, and relative standard deviation values of each spheroid, as previously described by Cristaldi and colleagues (Cristaldi et al., 2025).

2.3.4. CellTiter-Glo® 3D cell viability assay

3D cell viability was measured using the CellTiter-Glo® 3D Cell Viability Assay (Promega, Milan, Italy) 72 h after the treatments. Spheroids were removed from the 384 U plates and placed separately in single wells of a 96-well opaque culture plate (BD Falcon, Corning, Somerville, MA, USA). CellTiter-Glo® 3D reagent was added to each well and the luminescence signal was read after 30 min using the Glo-Max® bioluminescent reader (Promega).

2.3.5. Digital-droplet PCR (ddPCR)

ddPCR analysis was performed using QX600 Droplet Digital PCR System Biorad (Bio-Rad Laboratories, Hercules, CA, USA). RNA was extracted from the cells and retrotranscription was performed as previously described (Arienti et al., 2021). The ddPCR reaction mixture was prepared for each sample using β-actine as housekeeping. 20 µl of ddPCR reaction mixture and 70 µl of droplet generation oil were added on the cartridge in the designated wells. The rubber gasket was attached over the cartridge before placing it in the QX600 droplet generator. 40 µl from each of the wells with generated droplets were transferred in a new 96 wells plate. After all the samples were loaded, the plate was heat-sealed and PCR was performed. The analysis was performed using the QX Manager Standard Edition analysis software version 2.1.0.25.

2.3.6. Annexin/V-FITC apoptosis assay

To evaluate the rate of apoptosis, eBioscience Annexin V-FITC Apoptosis Detection Kit was used. Cells to test were detached and counted, then seeded and treated 24 h post-seeding. To identify cells actively undergoing apoptosis, treated and untreated cells were collected after 72 h, washed in PBS 1X and then incubated with 25 µL/mL Annexin V-FITC in binding buffer (Thermo Fisher Scientific, Waltham, MA, USA) for 10 min at room temperature in the dark. Immediately before flow cytometric analysis, 50 µL/mL of propidium iodide was added to discriminate between apoptotic and necrotic cells. Cells were then analyzed by flow cytometry and data were analyzed using FlowJo Software (Ashland, OR, USA): cells negative for apoptosis and necrosis are Annex-/PI-, cells undergoing early apoptosis are Annex+/PI-, cells in late apoptosis are Annex+/PI+, and death cells are Annex-/PI+. Flow cytometric analysis was performed using the Attune NxT Flow Cytometer (Invitrogen, Waltham, MA, USA), 10,000 events were collected for each replicate. Data analysis was performed using FlowJoTM V.10.10.0 software.

2.4. In vivo experiments

2.4.1. Generation of luciferase-expressing GBM cells for in vivo bioluminescence tracking

A third-generation lentiviral vector encoding firefly luciferase under a CMV promoter and a puromycin resistance marker (pLenti CMV Puro LUC, Addgene) was used to generate stably transduced patient-derived cells. Lentiviral particles were produced in HEK293T cells *via* lipid-based co-transfection with the vector and packaging plasmids. Viral supernatants were collected 48–72 h post-transfection, clarified, and filtered (0.45 µm). Target cells, seeded at ~70% confluence, were exposed to the virus at an optimized multiplicity of infection. After 12–24 h, the medium was replaced with standard culture medium, and cells were subjected to puromycin selection for 48–72 h to eliminate non-transduced cells, resulting in a polyclonal population of stably transduced, luciferase-expressing cells. Luciferase activity and stability were confirmed *in vitro* by luminescence measurement following D-luciferin incubation (Promega) using either the multimode microplate reader Synergy H1 (Biotek, USA) and IVIS system (IVIS Lumina III *in Vivo* Imaging System (Revvity, PerkinElmer), ensuring suitability for downstream bioluminescence tracking.

2.4.2. Animals

All animal experiments were approved by the Italian Ministry of

Health (Authorization No 02/2022-UT, 13 May 2022).

Eight-week-old male NOD/SCID mice (Inotiv, USA) were housed under specific pathogen-free (SPF) conditions with a 12 h:12 h light–dark cycle, 45% humidity, temperature of 22 ± 1 °C, and ad libitum access to food and water. Following initial *in vivo* optical imaging for tumor assessment, mice were randomly assigned to two experimental groups (n = 3 each) to balance starting tumor burden. Experiments began on day 7 after arrival, allowing for acclimatization. Animals were monitored daily, and body weight was recorded three times per week.

2.4.3. Surgical procedure and tumor cell implantation

On Day 0, mice were anesthetized with ketamine/xylazine and positioned in a stereotaxic frame. A small burr hole was drilled relative to bregma, and 2 μL of patient-derived GBM cell suspension (1×10^5 cells/μL in PBS) was injected into the striatum. The needle was left in place for 3 minutes to prevent reflux before withdrawal, the incision was sutured, and ophthalmic ointment was applied to reduce ocular stress. Post-operative analgesia was administered for 3 days, and animals were monitored daily for signs of discomfort.

2.4.4. Quantitative analysis of tumor growth by bioluminescence imaging

Tumor growth was monitored longitudinally using patient-derived cells engineered to constitutively express luciferase. Bioluminescent signal, generated upon intraperitoneal injection of D-luciferin (Revvity Inc., USA), correlates with tumor volume. Mice were anesthetized with isoflurane (4% induction, 1.5% maintenance) and placed on a thermoregulated pad within the IVIS III Lumina imaging system (Revvity Inc., USA). Imaging was performed weekly from one-week post-implantation until humane endpoint. Sequential luminescence measurements allowed indirect quantification of tumor formation, growth, and extension, and were compared with control animals.

2.4.5. Rotarod test

To assess motor and behavioral deficits associated with striatal GBM growth, mice were evaluated weekly using the Rotarod test. Animals were placed on a 3 cm-diameter rotating rod accelerating from 4 to 40 rpm over 5 minutes, with a platform 15 cm below to record falls. The primary endpoint was latency to fall, reflecting motor coordination and balance.

2.4.6. In vivo **RC-106**·HCl treatment protocol and experimental design

Tumor growth was first assessed on Day 7 post-implantation by bioluminescence imaging (IVIS). Upon confirmation of tumor engraftment, the first treatment cycle was started on Day 7. **RC-106** HCl was administered via the intraperitoneal route to ensure consistent systemic bioavailability and to circumvent potential first-pass metabolism. The treatment was performed for four weekly cycles, five consecutive days per week (Monday–Friday) with a 2-day weekend break, including a one-week mid-protocol interruption. Tumor progression was monitored weekly by IVIS imaging and Rotarod performance, with all procedures conducted according to humane endpoint criteria. Tumor growth was quantified as the mean fold change in total flux over the treatment period, as previously described (Sandri et al., 2021; Tesei et al., 2019).

Eight-week-old male NOD/SCID mice were randomly assigned to two groups:

- Vehicle Control (group 1, $n = 4$): received intraperitoneal vehicle injections.
- **RC-106**·HCl Treatment (group 2, $n = 5$): received **RC-106**·HCl at 22 mg/kg (corresponding at 20 mg/kg of **RC-106**) body weight *via* intraperitoneal injection (i.p.).

2.5. Pharmacokinetic and brain distribution studies

2.5.1. Animals and biological matrix preparation

Animals were treated as already described (Tesei et al., 2019). Briefly, male CD-1 mice ($n = 4$/time point) received an intraperitoneal administration (i.p., 10 mL/kg) of **RC-106**·HCl at 11 mg/kg (corresponding at 10 mg/kg of **RC-106**, a dose selected as well-tolerated and suitable for defining PK parameters while minimizing potential confounding factors associated with repeated dosing). CD-1 male mice were exsanguinated under anesthesia (isoflurane) from the aorta at the following time points: 5, 10, 30, 120, 240 and 480 min. Blood samples were collected in tubes containing heparin, gently mixed and immediately placed on ice and then centrifuged (3500 × *g*, at 4 °C for 15 min), the obtained plasma samples were collected and transferred to individually labeled tubes and frozen at −80 °C until the analysis. Brain was taken by surgical skull resection, washed in saline, dried on paper, weighted and frozen at −80 °C. The organs were homogenized using a Velp OV5 homogenizer with 20 mM ammonium formate buffer in a ratio of 1 g of tissue per 10 mL of buffer (assuming a brain tissue density of approximately 1 g/mL for comparison of brain and plasma concentrations).

2.5.2. Sample preparation and analysis

Plasma sample preparation was already described (Tesei et al., 2019). For the PK and tissues distribution sample analysis, plasma and brain homogenates samples (50 μL) were spiked in 200 μL of internal standard (I.S.) in MeOH (0.1 μg/mL of RC-33), followed by 2 min vortex mixing. Samples were centrifuged and transferred in glass vials; 5 μL aliquots of the collected samples were injected into the LC-MS/MS system. Standard calibration graphs were constructed by linear least-squares regression analysis on the analyte/I.S. area ratio plotted against sample concentration. Standard curves of **RC-106**·HCl were prepared for plasma and brain homogenate and analyzed together with each QC and unknown sample set. Standard calibration graphs were constructed by linear least-squares regression analysis on the analyte/IS area ratio plotted against sample concentration. Calibration ranges were from 5 to 1000 ng/mL for plasma and 2.5 to 1000 ng/mL for brain homogenate. Accuracy values were determined in triplicates at three different concentrations (high, medium, and low) in the range of linearity of the calibration curves.

2.6. Statistical analysis

In vitro assays were analyzed by applying the Student *t*-test for 2-group comparisons. Differences were considered significant at $p < 0.05$. All experiments were performed at least three times, and quantifiable data derived from three independent experiments and reported as mean ± standard deviation

For the *in vivo* experiments, comparisons were made using repeated measures analysis of variance (ANOVA), considering tumor growth, treatment (treated/control), time points (1wpi-6wpi), the 5 measurements for each mouse, and the interaction between treatment and time. Due to the exploratory nature of the study and the limited statistical power, a threshold of $p < 0.10$ was predefined for these experiments. Accordingly, p-values < 0.10 were considered indicative of statistical trends warranting further investigation, rather than definitive statistical significance. Statistical analysis for *in vitro* and *in vivo* experiments was carried out using GraphPad Prism 9 software (GraphPad Software, San Diego, CA, USA).

3. Results

3.1. Physisicochemical properties prediction

Physicochemical properties and ADMET profile were predicted using the open-access web tool ADMETlab 3.0 (freely available at https://admetlab3.scbdd.com/). This platform allows a assessment of pharmacokinetics and toxicity properties of small molecules, and an efficient preliminary prediction of their drug-likeness (Fu et al., 2024; Xiong et al., 2021). **RC-106**·HCl displays several favorable characteristics,

such as compliance to Lipinski's rule of 5 and the golden triangle physicochemical space, absence of structural alerts for Pan-Assay Interference Compounds (PAINS) scaffolds, and an overall good absorption and distribution (Baell, 2016; Dahlin et al., 2015; Johnson et al., 2009; Lipinski et al., 2012). Most importantly, it was predicted to be able to cross the BBB, and not to be a P-glycoprotein (Pgp) substrate. Moreover, the software predicted a favorable metabolism profile, in terms of stability to human liver microsomes, low interaction as Cytochromes P450 (CYP) substrate, and moderate plasma clearance in humans (8.44 mL/min/kg). These encouraging results prompted us to continue our investigations.

3.2. Scaled-up and eco-sustainable synthetic procedure for **RC-106**·HCl

Having previously optimised the synthetic route on hundreds-of-milligrams scale, we now developed an efficient scaling-up procedure to multi-grams scale that incorporates green chemistry principles. This allowed us to access to a sufficient amount of **RC-106**·HCl for a comprehensive biological characterization both *in vitro* and *in vivo*.

Specifically, the Mizoroki-Heck reaction was conducted using the commercial catalyst Pd EnCat® 40 (0.4mmol/g Pd load-ing), which consists of $Pd(OAc)_2$ supported on a poly-urea matrix, allowing an easier and safer handling and recovery (Scheme 1). The reaction was performed in refluxing ethanol overnight, using an air condenser to avoid water consumption. The crude product was filtered to remove the recyclable catalyst and dried. The solid was precipitated with Heptane (Hept) to remove the starting material and some side products. Automatic flash chromatography was employed for the complete purification of product 1. Subsequent hydrolysis of ester 1 afforded the corresponding carboxylic acid 2 as its sodium salt. The undissociated acid was extracted in DCM upon treatment with a solution of 1 M HCl. Although DCM is not a green solvent, preliminary screening of alternative solvents (ethyl acetate, diethyl ether, and MTBE) resulted in incomplete extraction and therefore were abandoned. Since the crude product contained stereo- and regio-isomers as byproducts (see Supplementary Material), several crystallization solvent systems were screened to selectively isolate the desired E isomer, using green solvent selection principles. A mixture of acetone and water (6:4) proved optimal, representing an environmentally benign solvent system providing compound 2 in suitable yield and purity (60% of yield and purity > 95%). Acid 2 was coupled with 4-benzylpiperidine using 2-(1H-benzotriazol-1-yl)-1,1,3,3-tetramethyluronium tetrafluoroborate (TBTU) and triethylamine (TEA) in DMF at room temperature overnight. Also in this case, alternatives to DMF were experimented (e.g., ACN and THF), but resulted in modest yields and/or higher impurities. However, this mild, ambient temperature protocol offers the advantage to eliminate the need for heating, reducing energy consumption, while giving compound 3 in quantitative yield upon isolation through liquid–liquid extraction (with ethyl acetate and water), avoiding chromatographic purification. The amide intermediate 3 was subsequently reduced to the tertiary amine RC-106 using $LiAlH_4$ in anhydrous DCM at room temperature in 40 min. The addition of trimethylsilyl chloride (TMSCl) allows to reduce reaction time to 40 min, and after completion, the reaction mixture was quenched with water and filtered through Celite to eliminate inorganic salts, with the aqueous waste containing only benign aluminum salts suitable for standard disposal. Final purification achieved by crystallization from hot EtOH eliminated the need for column chromatography, avoiding silica gel waste and multiple organic solvents typically required for purification. Conversion to the hydrochloride salt was conducted as the final step to improve both purity and water solubility of the target compound. Specifically, using HCl in diethylether, the hydrochloride salt precipitated, finally affording RC-106•HCl with 99% purity (HPLC-UV) and 16% overall yield.

3.3. Solid-State characterization of **RC-106**·HCl

RC-106·HCl powder samples were characterized using thermoanalytical techniques (TGA and DSC), X-ray powder diffraction (XRPD), Fourier-transform infrared (FT-IR) spectroscopy, and scanning electron microscopy (SEM).

Thermogravimetric Analysis (TGA) (Fig. 4) was performed under nitrogen atmosphere from 25 °C to 250 °C. The thermogram showed an initial weight loss of 0.5% starting at approximately 75 °C, attributed to the release of adsorbed water. Thermal degradation of **RC-106**·HCl began, with a very fast kinetics, at around 170 °C. By 250 °C, the sample had undergone a total mass loss of 22.84% and was rapidly decomposing.

Differential Scanning Calorimetry (DSC) analysis was carried out by heating the sample under argon flux in an open aluminum crucible from 25 °C to 250 °C at 5 °C/min, followed by cooling back to 25 °C at the same heating rate. The DSC thermogram exhibited a well-defined endothermic peak with an onset at 217 °C, consistent with melting accompanied and followed by decomposition, as supported by the TGA profile and the absence of thermal events upon cooling.

The FT-IR spectrum of **RC-106**·HCl displayed a multi-component band between 3100 cm^{-1} and 2900 cm^{-1} associated with C–H stretching from both aliphatic and olefinic groups. The complex intense peak between 2750 cm^{-1} and 2300 cm^{-1}, centered at 2515 cm^{-1}, can be attributed to the NH^+ Cl^-stretch, confirming the nature of hydrochloride salt of the obtained compound (Colthup et al., 1975). Distinct peaks between 1700 cm^{-1} and 1600 cm^{-1} and in the range 1350 cm^{-1} and 1250 cm^{-1} revealed the presence of C = C and C—N groups. Additionally, sharp features in the range 1400–1300 cm^{-1} were assigned to C—H bending and rocking modes.

XRPD analysis pointed out the highly crystalline nature of the sample, that is confirmed also by SEM analysis (Fig. 5), showing the formation of regular rods and platelets of consistent size.

In particular, the SEM analysis showed the presence of aggregates (in Fig. 5 is shown one selected example) consisting of rod- and platelet-like structures, with smooth prismatic surfaces, which seem grew from one common nucleation and crystallization point. Aggregates exhibited major axes up to 400 μm and minor axes up to 150 μm. Rods were up to 20 μm in length with cross-sections of ~10 μm, while platelets were rectangular prisms with major sides of approximately 10 μm. This

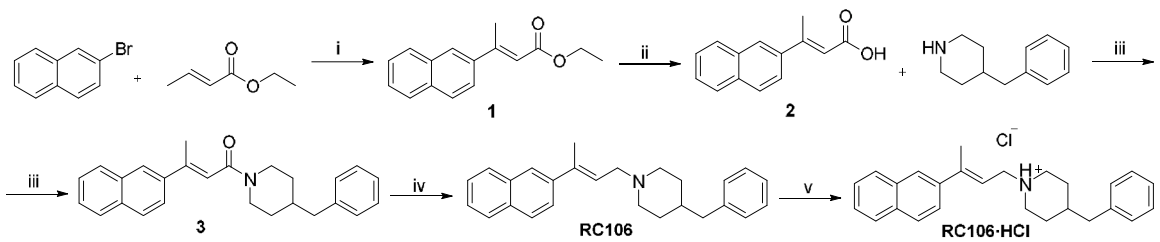

Scheme 1. Reagents and conditions: (i) TEAC (3.1 equiv.), AcONa dry (2.5 equiv.), Pd EnCat® 40 (0.8 mol.%), EtOH, 90 °C, overnight, 45% yield; (ii) NaOH 3 M (10 equiv.), EtOH/THF 3:1, 60% yield; (iii) 4-Benzyl piperidine (1.2 equiv.), TBTU (1.2 equiv.), TEA (2.4 equiv.), DMF, 0 °C-rt, 93% yield; (iv) TMSCl (1.2 equiv.), $LiAlH_4$ (1.5 equiv.), DCM, 0 °C-rt, 40′, 65% yield; (v) HCl in Et_2O (1 equiv.), Et_2O, rt, 2 h, 98% yield.

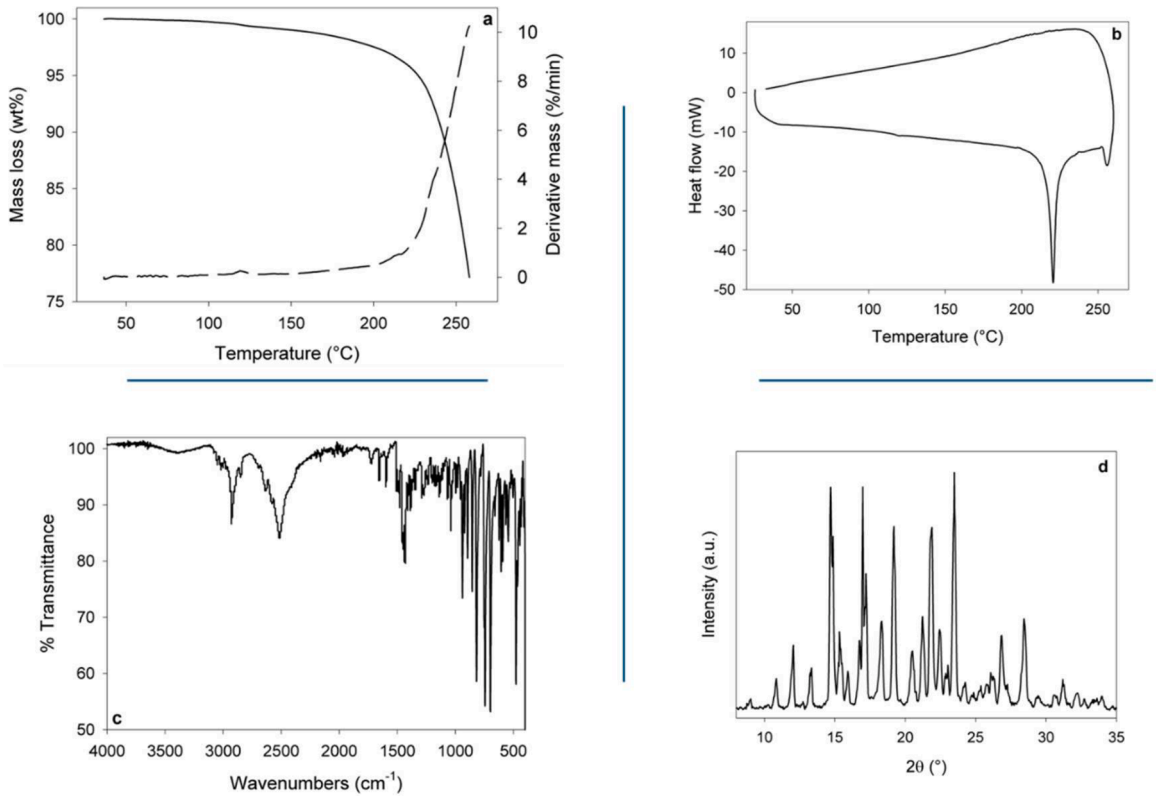

Fig. 4. Solid-state characterization of RC-106·HCl: (A) TGA analysis, (B) DSC analysis, (C) FT-IR spectroscopy, (D) XRPD analysis.

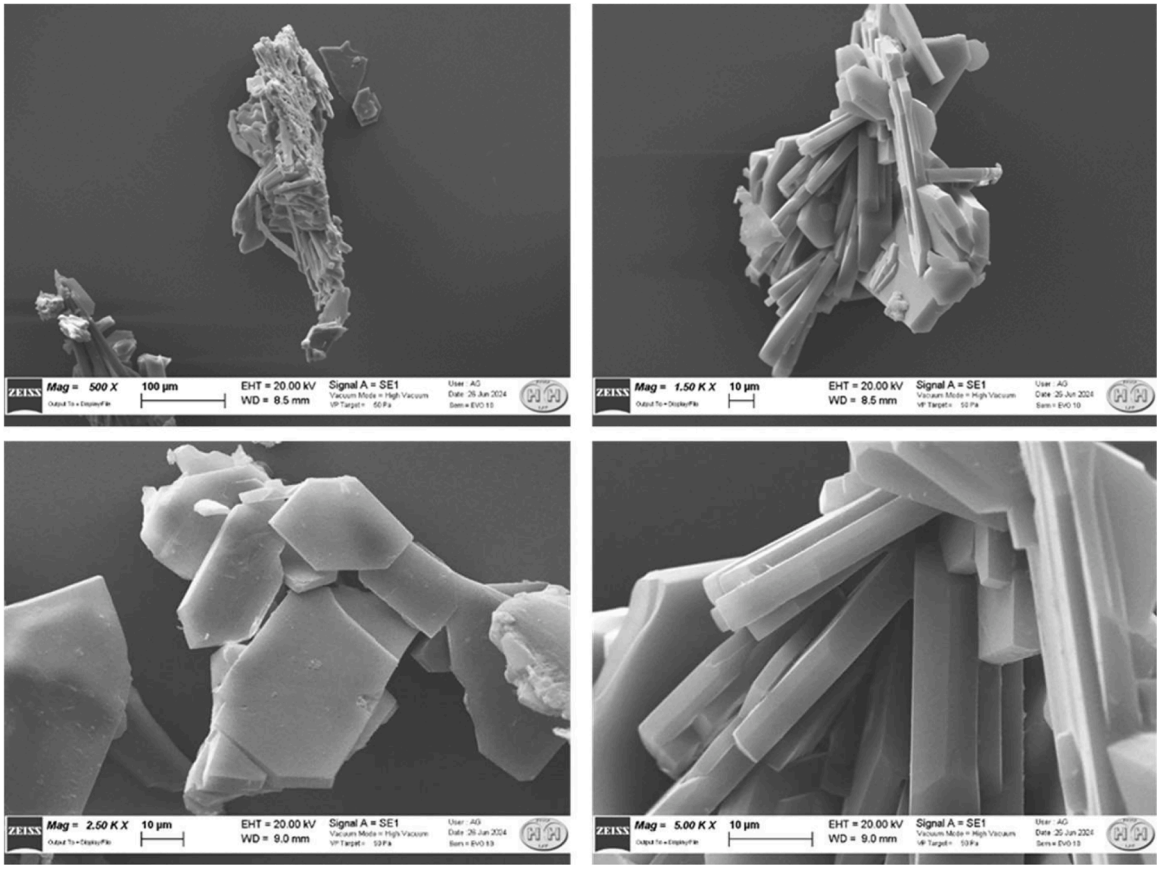

Fig. 5. SEM images of RC-106·HCl aggregates at different magnifications (from 500X to 5000 X).

particular morphology could be attributed to the developed preparative method (solvent) and the slow crystallization procedure, allowing the formation of crystals with regular shape and large faces (Gao et al., 2024).

3.4. *In vitro experiments*

3.4.1. *Efficacy in GBM commercial and patient-derived cell cultures*

Preliminary *in vitro* experiments were conducted on two commercial GBM cell lines (U87 and A172) grown as 2D monolayers, and on two patient-derived primary GBM cell lines (G34 and G48), which spontaneously grow as floating small neurospheres. To better reproduce the tumor microenvironment, all experiments were carried out under hypoxic conditions using a dedicated hypoxic cell incubator and a laminar flow cabinet with a modified atmosphere containing 1% oxygen. The expression of both S1R and S2R in all four cell lines was confirmed by Bio-Rad Droplet Digital™ PCR (ddPCR) (Fig. 6A and Fig. 7A). The cytotoxic activity of **RC-106**·HCl demonstrated its ability to induce cell killing independently of the GBM model used, with IC_{50} values ranging between 44 μM and 54 μM across all tested cell lines and primary neurospheres (Fig. 6B and Fig. 7B).

These findings were further confirmed by apoptosis analysis in U87 and A172 cells, which revealed a marked increase in total cell death (51.91% ± 8.28 in U87 and 27.77% ± 4.86 in A172 cells) and necrosis (45.03% ± 15.86 and 57.36% ± 8.55, respectively) after 48 h of treatment with **RC-106** at 50 μM (Fig. 7C). In addition, morphological examination of GBM primary cells grown as 3D spheroids (Ø ranging from 450 to 500 μm), showed a pronounced reduction in size and loss of structural compactness in both primary GBM models at the highest tested concentration (100 μM), particularly evident after 72 h of **RC-106** exposure (Fig. 7C). Density and diameter were assessed by W8 cytometer, to further investigate the impact of **RC-106** treatment on GBM neuro-spheroids. In particular, an increase in spheroid diameter (μm), together with a decrease in spheroid density (fg/μm^3), was observed with increasing treatment dose and exposure time. The demonstrated efficacy of **RC-106** in 3D glioma models, which represents a more advanced and physiologically relevant platform that better reproduces the tumor microenvironment, further supports its potential for translation to *in vivo* systems.

3.5. *PK and biodistribution*

Following intraperitoneal administration of **RC-106**·HCl (11 mg/kg), the compound exhibited a rapid absorption phase, reaching a plasma C_{max} of 973.3 ng/mL within 5 min and a brain C_{max} of 2219 ng/g after 10 min (Fig. 8). This early attainment of peak concentrations highlights the prompt systemic absorption of the compound and its efficient penetration into the central nervous system.

As summarized in Table 1, both plasma and brain concentration–time profiles declined rapidly, with elimination half-lives ($t_{1/2}$) of 202 min and 147 min, respectively. The relatively short $t_{1/2}$ values indicate a fast elimination rate, consistent with limited persistence in systemic circulation. Despite this rapid clearance, the AUC0-t brain/AUC0-t plasma ratio of approximately 5, calculated under the conventional assumption of a brain density of approximately 1 g/mL (Schültke, 2025), demonstrates a pronounced propensity of **RC-106**·HCl to distribute into brain tissue, supporting its ability to readily cross the blood–brain barrier.

The pharmacokinetic profile of **RC-106**·HCl, characterized by rapid absorption, short elimination half-life, and preferential brain distribution, supports its potential for CNS-targeted activity. Conversely, the limited systemic persistence may reduce peripheral exposure. Of note, these data were obtained following intraperitoneal administration; characterization of oral bioavailability and absolute systemic exposure following intravenous dosing remains to be addressed in future work.

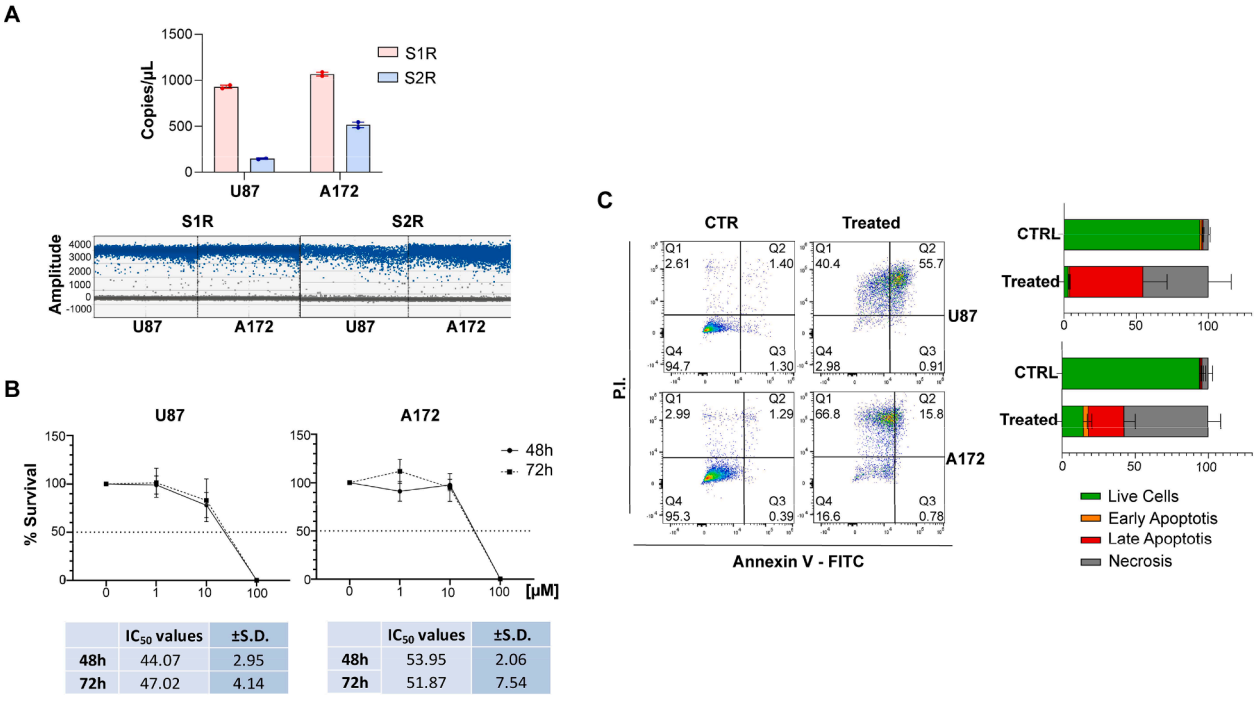

	IC_{50} values	±S.D.
48h	44.07	2.95
72h	47.02	4.14

	IC_{50} values	±S.D.
48h	53.95	2.06
72h	51.87	7.54

Fig. 6. 2-D experiments. (A) Expression of S1R and S2R genes in U87 and A172 GBM cell lines grown as 2D cell cultures. Gene expression was analyzed by Bio-Rad Droplet Digital™ PCR (ddPCR) and represents the mean of two independent biological replicates. (B) Cell viability assay. Viability of U87 and A172 cells was assessed using the Promega Cell Titer-Glo® assay after treatment with RC-106 at different concentrations and time exposures. (C) Apoptosis analysis by Annexin V assay. Cells were treated with RC-106 50μ M for 48 h. A representative flow cytometry dot plot graph is shown. The bar graphs show the mean percentage of apoptotic cells (Annexin V positive) from three independent experiments performed by different operators. P.I.= Propidium Iodide. All the cells were grown in a hypoxic atmosphere (Oxygen 1%).

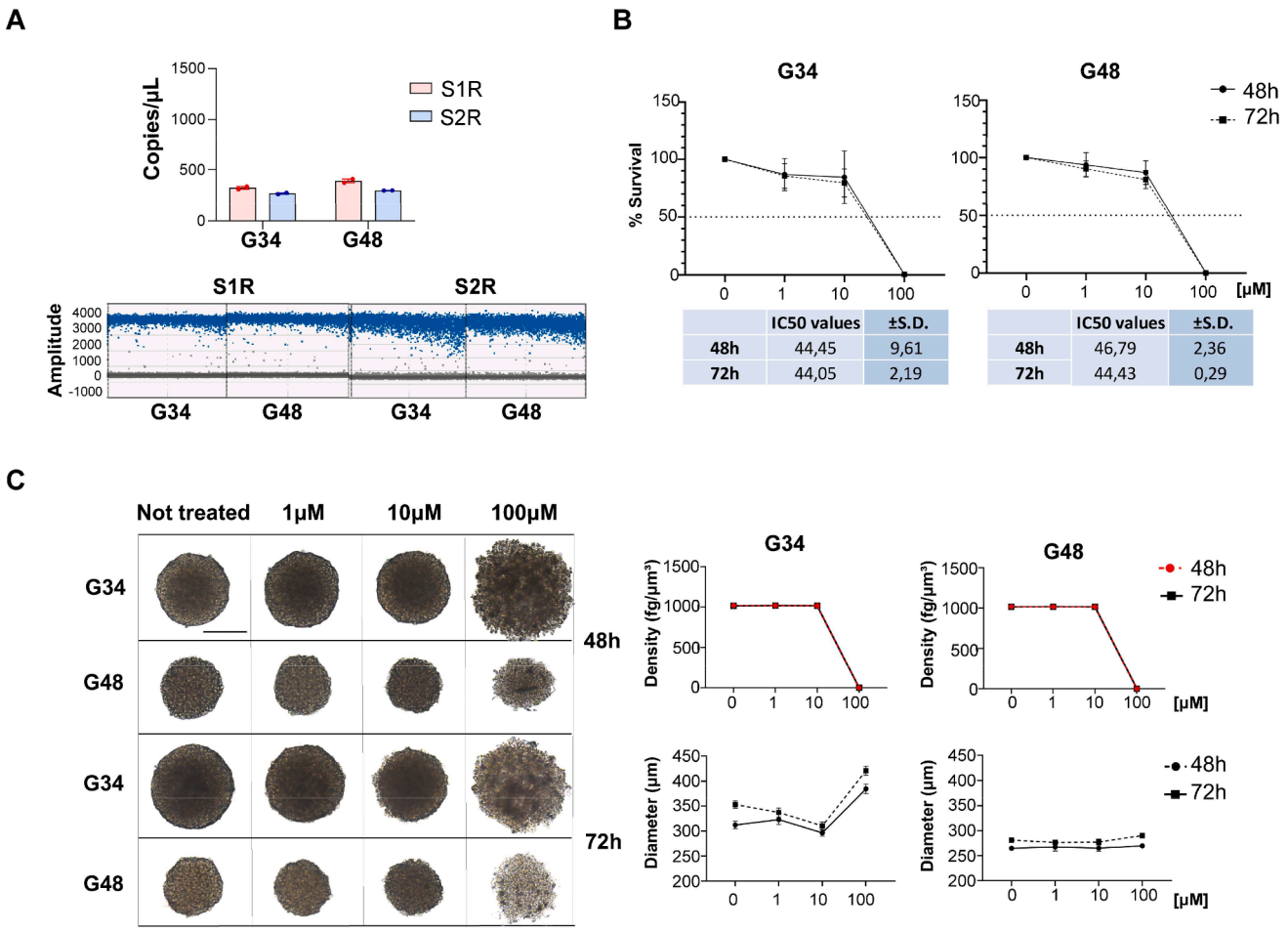

	IC50 values	±S.D.
48h	44,45	9,61
72h	44,05	2,19

	IC50 values	±S.D.
48h	46,79	2,36
72h	44,43	0,29

Fig. 7. 3D experiments. (A) Expression of S1R and S2R genes in G34 and G48 patient-derived GBM primary cell lines grown as 3D neurospheres in hypoxic atmosphere (Oxygen 1%). Gene expression was analyzed by ddPCR and represents the mean of two independent biological replicates. (B) Cell viability assay. RC-106 cytotoxic effect was assessed on G34 and G48 neurospheres by CellTiter-Glo® 3D Cell Viability Assay (Promega) after treatment with different concentrations and time exposures. (C) Disaggregation Analysis. Phase-contrast imaging of GBM neurospheres treated with RC-106 at different doses and time of exposures were carried out with an inverted Olympus IX51 microscope (Olympus Corporation, Tokyo, Japan), equipped with a Nikon Digital Sight DS-Vi1 camera (CCD vision sensor, square pixels of 4.4 µM side length, 1600 × 1200 pixel resolution, 8-bit grey level) (Nikon Instruments, Spa. Florence, Italy). The images are representative of at least three independent experiments. Scale bar: 200µ M.

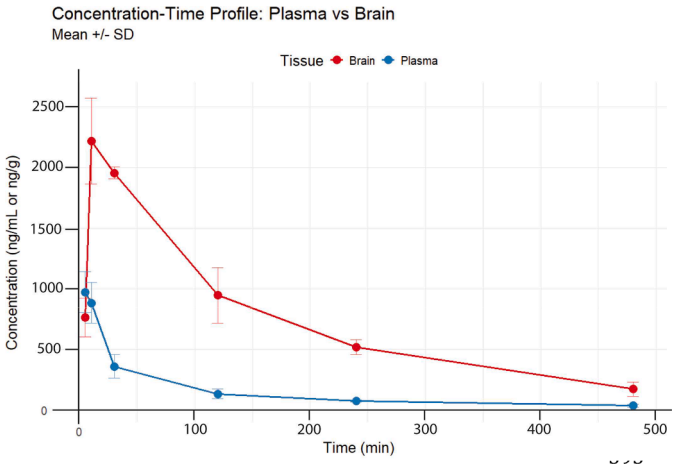

Fig. 8. Plasma and brain concentration–time profiles of RC-106·HCl following a single intraperitoneal dose of 11 mg/kg (corresponding to 10 mg/kg RC-106) in CD-1 mice ($n = 4$ per time point). Plasma concentrations are expressed as ng/mL and brain concentrations as ng/g (mean ± SD). For calculation of the brain-to-plasma AUC ratio (Kp), a brain tissue density of approximately 1 g/mL was assumed.

Table 1
Plasma pharmacokinetic and tissue distribution parameters of RC-106·HCl after IP administration at a dose of 10 mg/kg in mice ($n = 4$).

Pharmacokinetic parameters	Plasma	Brain
$AUC_{0\text{-}t}$ (ng/mL*min)	67,987	352,804
$t_{1/2}$ (min)	202	147
C_{max} (ng/mL or ng/g)	973	2219
T_{max} (min)	5	10

3.6. *In vivo experiments*

3.6.1. *PDOX GBM mouse model establishment and cells engraftment*

In vivo optical imaging (bioluminescence) confirmed the successful and highly reproducible establishment of the GBM Patient-derived orthotopic xenograft (PDOX) mouse model. As shown in Fig. 9, control (CTRL) mice exhibit no bioluminescence signal, whereas the tumor signal is clearly detectable in mice stereotaxically injected with patient-derived GBM cells (2×10^6 and 4×10^6 cells). A dose-dependent trend is also observed, with a more intense bioluminescence signal registered in mice that received the higher cell dose (4×10^6). This result validates the efficacy of the implantation protocol and the viability of the tumor cells in the mouse brain (Fig. 9A).

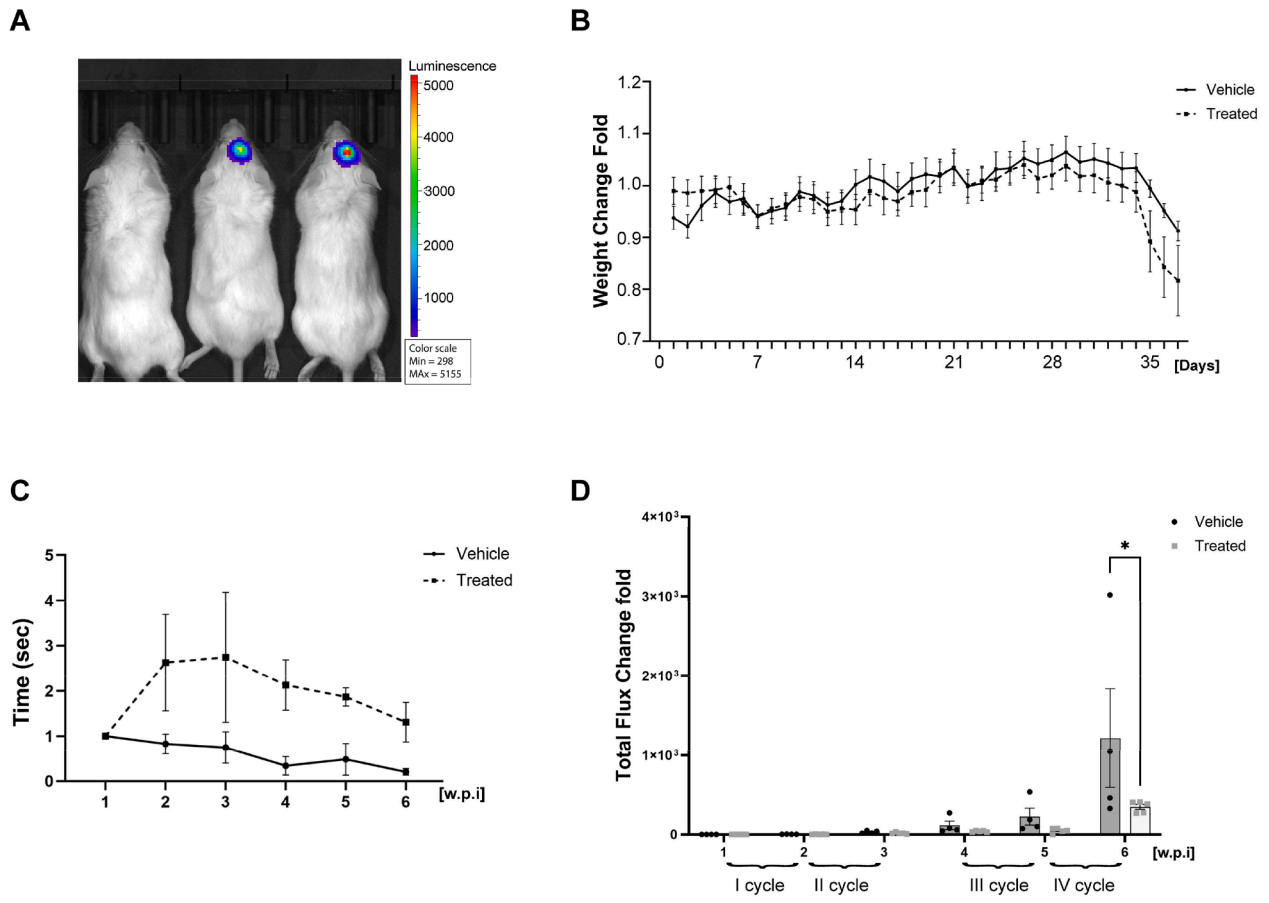

Fig. 9. *In vivo* evaluation of RC-106·HCl treatment efficacy. (A) The stereotaxic orthotopic injection of patient-derived GBM cells into the mouse brain was verified through *in vivo* optical imaging (Lumina III, Revvity s.r.l.). GBM patient-derived cell lines were previously genetically engineered with a lentiviral vector to constitutively express luciferase. Ten minutes after the i.p. injection of Luciferin substrate (Revvity, s.r.l.) Bioluminescence signals derived from tumor cells were evaluated. A PDOX mouse model of GBM was successfully established in a highly reproducible way. The figure shows the comparison between healthy CTRL mice (left) with the absence of signal, mice injected with 2×10^6 cells (middle) and mice injected with 4×10^6 cells (right), one week after surgery. (B) Body weight assessment during RC-106·HCl treatment. Longitudinal monitoring of mean fold change of daily body weight for RC-106·HCl treated mice ($n = 5$) and vehicle control mice ($n = 4$), recorded from the day of GBM cell inoculation over the period of observation. (C) Rotarod performance of mice over time. Longitudinal assessment of motor function using the Rotarod test. The curves represent the comparison of mice treated with RC-106·HCl ($n = 5$) and vehicle-treated control group ($n = 4$); w.p.i.=weeks post injection. (D) Efficacy of RC-106·HCl treatment on tumor progression. Graph illustrating the mean fold-change of total bioluminescence flux (photons/second) in the RC-106·HCl treated group (20 mg/kg), compared to the vehicle control group over the period of evaluation (6 weeks). The fold-change was calculated relative to the signal at week 1 (or baseline), for each time point. Data are presented as mean ± SEM of all mice in the group at different time points. Statistical analysis using a Two-way ANOVA revealed no significant differences in body weight or motor performances between groups across all time points ($p > 0.05$). Considering tumor growth, statistical analysis using a Two-way ANOVA for repeated measures analysis of variance revealed a significant treatment effect over time ($p < 0.10$), in vehicle-treated control mice compared with the RC-106•HCl-treated group, with the strongest effect observed at week 6 ($p < 0.05$).

3.6.2. *Animal weight monitoring*

To assess the safety and tolerability of the **RC-106**·HCl treatment (20 mg/kg), animal body weights were recorded daily, starting from the day of GBM cell inoculation. Fig. 9B shows the comparison between the mean ± SEM of body weight fold increase for vehicles ($n = 4$) and treated ($n = 5$) mice. Two-way ANOVA test was used for statistical analysis. Data indicate the treatment was well-tolerated, indicating no statistically significant overall difference in body weight progression ($p > 0.05$). In summary, the data indicate no significant negative effects of the **RC-106**·HCl treatment on animal body weight.

3.6.3. *Rotarod test*

Rotarod Test was assessed once a week, to compare the motor performances of treated ($n = 5$) and vehicle ($n = 4$) mice, to confirm that **RC-106**·HCl treatment does not affect the motor performance of mice. The mean scores (time in seconds) of the treated and vehicle groups were compared, as shown in Fig. 9C. The test confirmed the absence of neurotoxic effects following **RC-106**·HCl treatment. Furthermore, the data presented in Fig. 9C indicate a potential ameliorative effect of **RC-106**·HCl (20 mg/kg) on motor performance in GBM-bearing mice.

3.6.4. *Evaluation of the efficacy of **RC-106**·HCl treatment*

Mice were randomly divided into two groups. The treatment group ($n = 5$) received daily intraperitoneal (i.p.) injections of **RC-106**·HCl at a dose of 20 mg/kg body weight. The compound was dissolved in the vehicle composed of 5% DMSO, 5% Tween 80, and 90% sterile water. The treatment was administered daily for four weeks (5 days/week), with a one-week interruption mid-treatment. The control group ($n = 4$) was injected with the vehicle alone following the same administration schedule.

Tumor burden (Fig. 9D) was monitored weekly by longitudinal measurement of total bioluminescence flux. Despite the limited sample size, the analysis revealed a significant treatment effect over time ($p = 0.097$), in vehicle-treated control mice compared with the **RC-106**·HCl-treated group, with the strongest effect observed at week 6 ($p < 0.05$).

4. Discussion

Given that **RC-106**·HCl is intended for *in vivo* administration, obtaining multi-gram quantities in a safe, reproducible, and sustainable manner was fundamental to support preclinical studies. For this reason, a key aspect of this work was the translation of our previously reported small- and medium-scale syntheses (Rui et al., 2016; Tesei et al., 2019) into a scalable process, with an eye to green chemistry principles. Reducing hazardous reagents and solvents, optimizing reaction conditions to lower energy and water consumption, and simplifying purification steps contribute to the design of an eco-friendly synthesis. For each synthetic step, reaction parameters were specifically revised to minimize environmental impact without compromising efficiency. Attention was also devoted to purification, favoring crystallization or precipitation whenever feasible, with chromatography being employed only when strictly necessary using an automated system. The use of automated chromatography significantly reduces purification time, minimizes the environmental impact associated with silica consumption, and lowers solvent usage. In the Mizoroki–Heck reaction, the conventional use of DMF was replaced by EtOH as a safer and more environmentally friendly alternative. As recently reported by us, this system works well under microwave irradiation, allowing fast reaction times and improved yields (Rossino et al., 2024). However, considering the scale limitations of the available microwave reactor, in the present work, we employed reflux heating with an air condenser to minimize water consumption, despite the longer reaction time. Of note, our previously reported synthetic route to **RC-106** (Tesei et al., 2019) had a higher overall yield but suffered from poor scalability and sustainability. The main limitation consisted in the conversion of the allylic alcohol precursor in the final product *via* alkoxyphosphonium salts, according to the procedure described by Frøyen P. and Juvvik P. (Frøyen and Juvvik, 1995). This step involved the use of excess NBS and PPh_3 and the obtainment of triphenylphosphine oxide as by-product, entailing issues in terms of safety and ease of purification. In fact, the whole synthesis involved three chromatographic purifications (one for each step) (Tesei et al., 2019). Conversely, the new route to **RC-106** disclosed herein uses only one chromatographic separation and one filtration on Celite (despite having an additional synthetic step), prioritizing more scalable purification approaches such as crystallization, precipitation and liquid-liquid extraction. Thorough selection of the solvents for both reactions and purifications was also carried out, as it is known that they constitute the largest contribution to waste generation in synthetic processes in the pharmaceutical industry (Byrne et al., 2016; Kar et al., 2022). Thus, the present investigation constitutes a valuable starting point for the development of a truly scalable and sustainable synthesis of the target compound **RC-106**, although further improvements will be implemented in future optimization programs. One of the main goals will be the limitation of the formation of side-products, namely the isomeric materials obtained in the Heck and hydrolysis reactions (Figure S1). A more detailed characterization of all process-related impurities, required in later stages of development to enable full translation to GMP manufacturing, will be undertaken in subsequent studies. To sum up, the synthetic route developed represents a significant advance toward sustainable production of **RC-106**·HCl, balancing the demands of scale-up and environmental impact.

Once the target compound was obtained, solid-state characterization (XRPD, TGA/DSC, FT-IR, SEM) was undertaken since the knowledge of physico-chemical properties such as thermal stability, crystallinity, and morphology is fundamental per se and to explain properties such as solubility, dissolution ability, and possible chemical interactions. Compound **RC-106**·HCl was demonstrated to be highly crystalline and very stable at room temperature and up to at least 100 °C, without evident degradation or physical transitions.

Our data demonstrate consistent *in vitro* cytotoxicity of **RC-106**·HCl and confirm its brain penetration *in vivo* GBM models. The *in vivo* treatment schedule included a one-week interruption between dosing blocks, introduced to allow recovery from repeated intraperitoneal injections and to monitor potential delayed adverse effects. This conservative regimen may have further limited cumulative exposure compared with a continuous dosing protocol and is acknowledged as a limitation of the present study, to be addressed in future optimization of the treatment schedule. However, despite a significant time-dependent reduction of intracranial GBM burden, intraperitoneal administration of **RC-106**·HCl did not fully arrest tumor growth in our PDOX model. This observation is not unexpected when considered in light of the pharmacokinetic data. The maximal total brain concentration observed in mice (~6 μM, based on a Cmax of 2219 ng/g and assuming a brain density of 1 g/mL) remains substantially below the *in vitro* IC_{50} values determined in GBM cell models (44–54 μM), suggesting that brain exposures did not reach the concentration range associated with robust cytotoxic activity *in vitro*. The limited antitumor effect observed *in vivo* is therefore consistent with a sub-therapeutic exposure window rather than with a lack of intrinsic activity.

Several factors may further explain this exposure-efficacy gap. Pharmacokinetic analysis revealed rapid clearance and a relatively short elimination half-life, indicating that brain concentrations were unlikely to be sustained at pharmacologically relevant levels for a sufficient duration. Consistent with this interpretation, a higher dose (20 mg/kg) was evaluated in the efficacy studies to explore antitumor activity under conditions of increased systemic and brain exposure. Additionally, the *in vitro* IC_{50} values (44–54 μM) were determined under standard culture conditions and likely reflect sensitivity to prolonged or repeated drug exposure; the current dosing regimen may not have replicated these conditions *in vivo*. Finally, the highly aggressive nature of the patient-derived orthotopic xenograft model, combined with known differences in drug sensitivity between 2D/3D *in vitro* systems and the complex *in vivo* tumor microenvironment, may have further contributed to the observed efficacy gap.

The present study should therefore be viewed as an initial characterization of brain penetration and pharmacodynamic activity in a clinically relevant model. Future work will focus on optimizing dose and schedule, exploring formulation strategies to enhance CNS retention, and more rigorously defining the exposure–response relationship, with the aim of achieving brain concentrations within the *in vitro* potency range.

5. Conclusion

This study established **RC-106**·HCl as a scalable, pharmaceutically characterized pan-SRs modulator with a favorable preclinical safety profile and demonstrated GBM cytotoxicity. Sustainable synthesis yields high-purity **RC-106**·HCl with confirmed physicochemical stability, while consistent antiproliferative activity (IC_{50} 44–54 μM) across 2D and 3D patient-derived GBM models, coupled with apoptosis induction and neurosphere disruption under hypoxic conditions, supports Sigma receptors as therapeutically relevant targets in GBM.

These results establish the brain-penetrant properties of **RC-106**·HCl and provide a preliminary pharmacokinetic framework for CNS-targeted development. The observed brain/plasma AUC ratio of 5 constitutes a proof of concept for CNS distribution. Daily administration (20 mg/kg) in PDOX mice confirmed brain penetration and excellent tolerability without systemic or neurological toxicity. However, the absence of tumor reduction in this model reveals a critical translational gap: despite CNS penetration and *in vitro* potency, the exposure achieved *in vivo* was likely sub-therapeutic, possibly due to rapid clearance, limited accumulation, and/or metabolic inactivation, and thus insufficient to sustain effective tumor growth control. Whether the free brain concentrations achieved are sufficient to sustain pharmacodynamically relevant target engagement, it will require determination of the cerebral unbound fraction ($f_{u,brain}$) and formal exposure–response characterization, which represent logical next steps in the translational development of this compound.

Taken together, these findings position **RC-106** as a biologically validated lead with proof-of-concept for Sigma receptors modulation in GBM, while underscoring that brain penetration alone is insufficient to guarantee efficacy. Pharmaceutical optimization through preparation of alternative salts, improved formulations, alternative delivery strategies, or prodrug approaches, along with refined dosing regimens will be essential to bridge the exposure gap and fully explore the therapeutic potential of **RC-106** in clinically oriented studies.

Funding

This work was partly supported thanks to the contribution of Ricerca Corrente by the Italian Ministry of Health within the research line "Translational and Clinical Studies in Precision Oncology" and by the Italian Ministry of University and Research - PRIN 2022 "A Sustainable Approach for the Discovery of MultitaRgEt Agents against GlioblastoMa (SUS-DREAM)", project code: 20225XTNZE, CUP 20225XTNZE. NextGenerationEU.

CRediT authorship contribution statement

Noemi Marino: Writing – review & editing, Writing – original draft, Visualization, Validation, Methodology, Investigation, Formal analysis, Data curation, Conceptualization. **Roberta Listro:** Writing – review & editing, Writing – original draft, Visualization, Validation, Methodology, Investigation, Formal analysis, Data curation, Conceptualization. **Chiara Milanese:** Writing – review & editing, Validation, Methodology, Investigation, Formal analysis, Conceptualization. **Martina Bedeschi:** Writing – review & editing, Methodology. **Elena Cavassi:** Writing – review & editing, Methodology. **Carolina Palazzi:** Writing – review & editing, Methodology. **Marco Cambiaghi:** Writing – review & editing, Supervision. **Mario Rosario Buffelli:** Writing – review & editing, Supervision. **Fabio Nicolini:** Methodology. **Giulio Massimo Dondio:** Writing – review & editing, Conceptualization. **Giacomo Rossino:** Writing – review & editing, Methodology. **Pasquale Linciano:** Writing – review & editing, Methodology. **Daniela Rossi:** Writing – review & editing, Methodology. **Simona Collina:** Writing – review & editing, Visualization, Validation, Supervision, Software, Resources, Project administration, Methodology, Investigation, Funding acquisition, Formal analysis, Data curation, Conceptualization. **Anna Tesei:** Writing – review & editing, Visualization, Validation, Supervision, Software, Resources, Project administration, Methodology, Investigation, Funding acquisition, Formal analysis, Data curation, Conceptualization.

Declaration of competing interest

The authors declare no competing financial interest.

Acknowledgements

The authors would like to thank the Centro Grandi Strumenti, University of Pavia, for access to the Bruker Avance 400 MHz NMR spectrometer and for the technical assistance provided during this work.

Supplementary materials

Supplementary material associated with this article can be found, in the online version, at doi:10.1016/j.ejps.2026.107519.

Data availability

Data will be made available on request.

References

Arienti, C., Pignatta, S., Zanoni, M., Zamagni, A., Cortesi, M., Sarnelli, A., Romeo, A., Arpa, D., Longobardi, P., Bartolini, D., Tosatto, L., Naldini, A., Tesei, A., 2021. High-pressure oxygen rewires glucose metabolism of patient-derived glioblastoma cells and fuels inflammasome response. Cancer Lett. 506, 152–166. https://doi.org/10.1016/j.canlet.2021.02.019.

Baell, J.B., 2016. Feeling Nature's PAINS: natural products, natural product drugs, and pan assay interference compounds (PAINS). J. Nat. Prod. 79, 616–628. https://doi.org/10.1021/acs.jnatprod.5b00947.

Byrne, F.P., Jin, S., Paggiola, G., Petchey, T.H.M., Clark, J.H., Farmer, T.J., Hunt, A.J., Robert McElroy, C., Sherwood, J., 2016. Tools and techniques for solvent selection: green solvent selection guides. Sustain. Chem. Process. 4, 7. https://doi.org/10.1186/s40508-016-0051-z.

Collina, S., Bignardi, E., Rui, M., Rossi, D., Gaggeri, R., Zamagni, A., Cortesi, M., Tesei, A., 2017. Are sigma modulators an effective opportunity for cancer treatment? A patent overview (1996-2016). Expert Opin. Ther. Pat. 27, 565–578. https://doi.org/10.1080/13543776.2017.1276569.

\Colthup, N.B., Daly, L.H., Wiberley, S.E., 1975. Introduction to infrared and Raman spectroscopy, 2nd ed. Academic Press, New York.

Cortesi, M., Zamagni, A., Pignatta, S., Zanoni, M., Arienti, C., Rossi, D., Collina, S., Tesei, A., 2020. Pan-Sigma receptor modulator RC-106 induces terminal unfolded protein response In *In vitro* pancreatic cancer model. Int. J. Mol. Sci. 21, 9012. https://doi.org/10.3390/ijms21239012.

Cristaldi, D.A., Bedeschi, M., Cavallaro, G., Sargenti, A., Pasqua, S., Bonetti, S., Gazzola, D., Marino, N., Fortuna, C.G., Tesei, A., 2025. Redefine tumor spheroids heterogeneity via PCA-coupled biophysical characterization. Sci. Rep. 15, 35632. https://doi.org/10.1038/s41598-025-19557-8.

Dahlin, J.L., Nissink, J.W.M., Strasser, J.M., Francis, S., Higgins, L., Zhou, H., Zhang, Z., Walters, M.A., 2015. PAINS in the assay: chemical mechanisms of assay interference and promiscuous enzymatic inhibition observed during a sulfhydryl-scavenging HTS. J. Med. Chem. 58, 2091–2113. https://doi.org/10.1021/jm5019093.

Di Nunno, V., Franceschi, E., Tosoni, A., Gatto, L., Lodi, R., Bartolini, S., Brandes, A.A., 2021. Glioblastoma: emerging treatments and novel trial designs. Cancers 13, 3750. https://doi.org/10.3390/cancers13153750.

Fallica, A.N., Pittalà, V., Modica, M.N., Salerno, L., Romeo, G., Marrazzo, A., Helal, M.A., Intagliata, S., 2021. Recent advances in the development of Sigma receptor ligands as cytotoxic agents: a medicinal chemistry perspective. J. Med. Chem. 64, 7926–7962. https://doi.org/10.1021/acs.jmedchem.0c02265.

Fonkem, E., Rogers, K.Newell, Tobin, R., Das, M., Bowen, S., Tadipatri, R., Healey, D., Quarles, C., Clark, J., 2022. DDEL-08. NOVEL combination therapy using Pi3kinase inhibition and immune based therapy for the treatment of Glioblastoma Multiforme. Neuro Oncol. 24, vii95. https://doi.org/10.1093/neuonc/noac209.354.

Frøyen, P., Juvvik, P., 1995. One-pot synthesis of secondary or tertiary amines from alcohols and amines via alkoxyphosphonium salts. https://doi.org/10.1016/0040-4039(95)02046-2.

Fu, L., Shi, S., Yi, J., Wang, N., He, Y., Wu, Z., Peng, J., Deng, Y., Wang, W., Wu, C., Lyu, A., Zeng, X., Zhao, W., Hou, T., Cao, D., 2024. ADMETlab 3.0: an updated comprehensive online ADMET prediction platform enhanced with broader coverage, improved performance, API functionality and decision support. Nucleic Acids Res. 52, W422–W431. https://doi.org/10.1093/nar/gkae236.

Gao, Y., Song, W., Yang, J., Ji, X., Wang, N., Huang, X., Wang, T., Hao, H., 2024. Crystal morphology prediction models and regulating methods. Crystals 14, 484. https://doi.org/10.3390/cryst14060484.

Georgiadis, M.-O., Karoutzou, O., Foscolos, A.-S., Papanastasiou, I., 2017. Sigma receptor (σR) ligands with antiproliferative and anticancer activity. Molecules 22, E1408. https://doi.org/10.3390/molecules22091408.

Grönros, J., Li, S., Ba, M., Wang, Z., Cao, L., Zhang, M., Ji, X., Guo, Z., Zhang, H., Gao, S., Liang, Z., Gan, L.-M., 2024. 486P Effects of a BBB-penetrating oligonucleotide drug, RBD8088, in mouse models of human glioblastoma. Ann. Oncol. 35, S422. https://doi.org/10.1016/j.annonc.2024.08.555.

Hotchkiss, K.M., Karschnia, P., Schreck, K.C., Geurts, M., Cloughesy, T.F., Huse, J., Duke, E.S., Lathia, J., Ashley, D.M., Nduom, E.K., Long, G., Singh, K., Chalmers, A., Ahluwalia, M.S., Heimberger, A., Bagley, S., Todo, T., Verhaak, R., Kelly, P.D., Hervey-Jumper, S., de Groot, J., Patel, A., Fecci, P., Parney, I., Wykes, V., Watts, C., Burns, T.C., Sanai, N., Preusser, M., Tonn, J.C., Drummond, K.J., Platten, M., Das, S., Tanner, K., Vogelbaum, M.A., Weller, M., Whittle, J.R., Berger, M.S., Khasraw, M., 2024. A brave new framework for glioma drug development. Lancet Oncol. 25, e512–e519. https://doi.org/10.1016/S1470-2045(24)00190-6.

invIOs, 2025. Press release: Invios Reports Promising Phase 1b Results For Cell Therapy APN401 in Advanced Solid Tumors. invIOs. –URL. https://www.invios.com/press-release-invios-reports-promising-phase-1b-results-for-cell-therapy-apn401-in-advanced-solid-tumors/. accessed 11.26.25.

IQVIA, 2025. Global Oncology Trends 2025: Adopting new Therapies As Modalities Shift and Expenditures Rise. IQVIA. https://www.iqvia.com/insights/the-iqvia-institute/reports-and-publications/reports/global-oncology-trends-2025.

Johnson, T.W., Dress, K.R., Edwards, M., 2009. Using the Golden Triangle to optimize clearance and oral absorption. Bioorg. Med. Chem. Lett. 19, 5560–5564. https://doi.org/10.1016/j.bmcl.2009.08.045.

Kar, S., Sanderson, H., Roy, K., Benfenati, E., Leszczynski, J., 2022. Green chemistry in the synthesis of pharmaceuticals. Chem. Rev. 122, 3637–3710. https://doi.org/10.1021/acs.chemrev.1c00631.

Katsushima, K., Natsume, A., Ohka, F., Shinjo, K., Hatanaka, A., Ichimura, N., Sato, S., Takahashi, S., Kimura, H., Totoki, Y., Shibata, T., Naito, M., Kim, H.J., Miyata, K., Kataoka, K., Kondo, Y., 2016. Targeting the Notch-regulated non-coding RNA TUG1

for glioma treatment. Nat. Commun. 7, 13616. https://doi.org/10.1038/ncomms13616.
Lazzarini, E., Silvestris, D.A., Benvenuto, G., Osti, D., Fattore, L., Paterra, R., Finocchiaro, G., Malatesta, P., Daga, A., Gallotti, A.L., Galli, R., Pelicci, G., Tesei, A., Bedeschi, M., Pallini, R., Pasqualini, L., Romualdi, C., Gallo, A., Ricci-Vitiani, L., Indraccolo, S., 2023. Genome-wide profiling of patient-derived glioblastoma stem-like cells reveals recurrent genetic and transcriptomic signatures associated with brain tumors. J. Neurooncol. 163, 47–59. https://doi.org/10.1007/s11060-023-04287-6.
Lipinski, C.A., Lombardo, F., Dominy, B.W., Feeney, P.J., 2012. Experimental and computational approaches to estimate solubility and permeability in drug discovery and development settings. Adv. Drug Deliv. Rev. 64, 4–17. https://doi.org/10.1016/j.addr.2012.09.019.
Listro, R., Stotani, S., Rossino, G., Rui, M., Malacrida, A., Cavaletti, G., Cortesi, M., Arienti, C., Tesei, A., Rossi, D., Di Giacomo, M., Miloso, M., Collina, S., 2020. Exploring the RC-106 chemical space: design and synthesis of novel (E)-1-(3-arylbut-2-en-1-yl)-4-(substituted) piperazine derivatives as potential anticancer agents. Front. Chem. 8, 495. https://doi.org/10.3389/fchem.2020.00495.
Liu, C.-C., Yu, C.-F., Wang, S.-C., Li, H.-Y., Lin, C.-M., Wang, H.-H., Abate, C., Chiang, C.-S., 2019. Sigma-2 receptor/TMEM97 agonist PB221 as an alternative drug for brain tumor. BMC Cancer 19, 473. https://doi.org/10.1186/s12885-019-5700-7.
Louis, D.N., Perry, A., Wesseling, P., Brat, D.J., Cree, I.A., Figarella-Branger, D., Hawkins, C., Ng, H.K., Pfister, S.M., Reifenberger, G., Soffietti, R., von Deimling, A., Ellison, D.W., 2021. The 2021 WHO Classification of Tumors of the Central Nervous System: a summary. Neuro Oncol. 23, 1231–1251. https://doi.org/10.1093/neuonc/noab106.
Magnaghi, P., Casuscelli, F., Ardini, E., Parazzoli, A., Troiani, S., Valsasina, B., Texido, G., Casale, E., Avanzi, N., Orsini, P., Nuvoloni, S., Salom, B., Borgia, A.L., Salsi, E., Saturno, G.S., Depaolini, S.R., Stellato, C., Montagnoli, A., Galvani, A., Isacchi, A., 2022. NMS-173, a potent, covalent second generation IDH1/IDH2 inhibitor. Eur. J. Cancer 174, S17. https://doi.org/10.1016/S0959-8049(22)00847-4.
Mandel, J.J., Yust-Katz, S., Patel, A.J., Cachia, D., Liu, D., Park, M., Yuan, Y., Kent, T.A., de Groot, J.F., 2018. Inability of positive phase II clinical trials of investigational treatments to subsequently predict positive phase III clinical trials in glioblastoma. Neuro Oncol. 20, 113–122. https://doi.org/10.1093/neuonc/nox144.
Mustang Bio, Inc., 2025. Mustang Bio Granted Orphan Drug Designation by U.S. FDA for MB-101 (IL13Ra2-targeted CAR T-cells) to Treat Astrocytomas and Glioblastoma [WWW Document]. Mustang Bio, Inc. URL. https://ir.mustangbio.com/news-events/press-releases/detail/192/mustang-bio-granted-orphan-drug-designation-by-u-s-fda-for. Accessed 11.26.25.
Nabors, L.B., Portnow, J., Ahluwalia, M., Baehring, J., Brem, H., Brem, S., Butowski, N., Campian, J.L., Clark, S.W., Fabiano, A.J., Forsyth, P., Hattangadi-Gluth, J., Holdhoff, M., Horbinski, C., Junck, L., Kaley, T., Kumthekar, P., Loeffler, J.S., Mrugala, M.M., Nagpal, S., Pandey, M., Parney, I., Peters, K., Puduvalli, V.K., Robins, I., Rockhill, J., Rusthoven, C., Shonka, N., Shrieve, D.C., Swinnen, L.J., Weiss, S., Wen, P.Y., Willmarth, N.E., Bergman, M.A., Darlow, S.D., 2020. Central Nervous System Cancers, Version 3.2020, NCCN Clinical Practice Guidelines in Oncology. J. Natl. Compr. Cancer Netw. 18, 1537–1570. https://doi.org/10.6004/jnccn.2020.0052.
Noorani, I., de la Rosa, J., 2023. Breaking barriers for glioblastoma with a path to enhanced drug delivery. Nat. Commun. 14, 5909. https://doi.org/10.1038/s41467-023-41694-9.
Oyer, H.M., Sanders, C.M., Kim, F.J., 2019. Small-molecule modulators of Sigma1 and Sigma2/TMEM97 in the context of cancer: foundational concepts and emerging themes. Front. Pharmacol. 10.
Peirsman, A., Blondeel, E., Ahmed, T., Anckaert, J., Audenaert, D., Boterberg, T., Buzas, K., Carragher, N., Castellani, G., Castro, F., Dangles-Marie, V., Dawson, J., De Tullio, P., De Vlieghere, E., Dedeyne, S., Depypere, H., Diosdi, A., Dmitriev, R.I., Dolznig, H., Fischer, S., Gespach, C., Goossens, V., Heino, J., Hendrix, A., Horvath, P., Kunz-Schughart, L.A., Maes, S., Mangodt, C., Mestdagh, P., Michlíková, S., Oliveira, M.J., Pampaloni, F., Piccinini, F., Pinheiro, C., Rahn, J., Robbins, S.M., Siljamäki, E., Steigemann, P., Sys, G., Takayama, S., Tesei, A., Tulkens, J., Van Waeyenberge, M., Vandesompele, J., Wagemans, G., Weindorfer, C., Yigit, N., Zablowsky, N., Zanoni, M., Blondeel, P., De Wever, O., 2021. MISpheroID: a knowledgebase and transparency tool for minimum information in spheroid identity. Nat. Methods 18, 1294–1303. https://doi.org/10.1038/s41592-021-01291-4.
Rawling, M.J., Ray-Sinha, A., Bestwick, M., Carter, M.K., Chahal, S.K., Chalmers, A.J., Elsey, D.J., Giddings, A., Gold, J., Henderson, S.H., MacGregor, C., Malcolm, A., Ortega, F., Phelan, A., Savory, E.D., Schwartz, A.C., Stevenson, N.G., Turner, E.L., Vass, M., Wright, J.A., Watson, C., 2025. Discovery of a potent, selective, and brain-penetrant checkpoint kinase 1 inhibitor, BEN-28010, for the treatment of glioblastoma. J. Med. Chem. 68, 9101–9125. https://doi.org/10.1021/acs.jmedchem.5c00279.
Rossino, G., Marrubini, G., Brindisi, M., Granje, M., Linciano, P., Rossi, D., Collina, S., 2024. A green Heck reaction protocol towards trisubstituted alkenes, versatile pharmaceutical intermediates. Front. Chem. 12, 1431382.
Rui, M., Rossi, D., Marra, A., Paolillo, M., Schinelli, S., Curti, D., Tesei, A., Cortesi, M., Zamagni, A., Laurini, E., Pricl, S., Schepmann, D., Wűnsch, B., Urban, E., Pace, V., Collina, S., 2016. Synthesis and biological evaluation of new aryl-alkyl(alkenyl)-4-benzylpiperidines, novel Sigma Receptor (SR) modulators, as potential anticancer-agents. Eur. J. Med. Chem. 124, 649–665. https://doi.org/10.1016/j.ejmech.2016.08.067.
Sandri, A., Lleo, M.M., Signoretto, C., Boaretti, M., Boschi, F., 2021. Protease inhibitors elicit anti-inflammatory effects in CF mice with Pseudomonas aeruginosa acute lung infection. Clin. Exp. Immunol. 203, 87–95. https://doi.org/10.1111/cei.13518.
Sarkaria, J.N., Hu, L.S., Parney, I.F., Pafundi, D.H., Brinkmann, D.H., Laack, N.N., Giannini, C., Burns, T.C., Kizilbash, S.H., Laramy, J.K., Swanson, K.R., Kaufmann, T. J., Brown, P.D., Agar, N.Y.R., Galanis, E., Buckner, J.C., Elmquist, W.F., 2018. Is the blood-brain barrier really disrupted in all glioblastomas? A critical assessment of existing clinical data. Neuro Oncol. 20, 184–191. https://doi.org/10.1093/neuonc/nox175.
Schaff, L.R., Mellinghoff, I.K., 2023. Glioblastoma and other primary brain malignancies in adults: a review. JAMA 329, 574–587. https://doi.org/10.1001/jama.2023.0023.
Schültke, E., 2025. Biomimetic phantoms in X-ray-based radiotherapy research: a narrative review. Biomimetics 10, 794. https://doi.org/10.3390/biomimetics10120794.
Seo, K., Ozawa, T., Raleigh, D.R., Nagatani, S., Hazama, M., 2025. Abstract 3043: preclinical efficacy assessment of brincidofovir against glioblastoma. Cancer Res. 85, 3043. https://doi.org/10.1158/1538-7445.AM2025-3043.
Shah, H.A., Mishra, A., Gouzoulis, M.J., Ben-Shalom, N., D'Amico, R.S., 2022. Analysis of factors leading to early termination in glioblastoma-related clinical trials. J. Neurooncol. 158, 489–495. https://doi.org/10.1007/s11060-022-04039-y.
Stupp, R., Mason, W.P., van den Bent, M.J., Weller, M., Fisher, B., Taphoorn, M.J.B., Belanger, K., Brandes, A.A., Marosi, C., Bogdahn, U., Curschmann, J., Janzer, R.C., Ludwin, S.K., Gorlia, T., Allgeier, A., Lacombe, D., Cairncross, J.G., Eisenhauer, E., Mirimanoff, R.O., European Organisation for Research and Treatment of Cancer Brain Tumor and Radiotherapy Groups, National Cancer Institute of Canada Clinical Trials Group, 2005. Radiotherapy plus concomitant and adjuvant temozolomide for glioblastoma. N. Engl. J. Med. 352, 987–996. https://doi.org/10.1056/NEJMoa043330.
Tesei, A., Cortesi, M., Pignatta, S., Arienti, C., Dondio, G.M., Bigogno, C., Malacrida, A., Miloso, M., Meregalli, C., Chiorazzi, A., Carozzi, V., Cavaletti, G., Rui, M., Marra, A., Rossi, D., Collina, S., 2019. Anti-tumor efficacy assessment of the Sigma Receptor Pan modulator RC-106. A promising therapeutic tool for pancreatic cancer. Front. Pharmacol. 10, 490. https://doi.org/10.3389/fphar.2019.00490.
Tesei, A., Cortesi, M., Zamagni, A., Arienti, C., Pignatta, S., Zanoni, M., Paolillo, M., Curti, D., Rui, M., Rossi, D., Collina, S., 2018. Sigma receptors as endoplasmic reticulum stress "gatekeepers" and their modulators as emerging new weapons in the fight against cancer. Front. Pharmacol. 9, 711. https://doi.org/10.3389/fphar.2018.00711.
Vanderbeek, A.M., Rahman, R., Fell, G., Ventz, S., Chen, T., Redd, R., Parmigiani, G., Cloughesy, T.F., Wen, P.Y., Trippa, L., Alexander, B.M., 2018. The clinical trials landscape for glioblastoma: is it adequate to develop new treatments? Neuro Oncol. 20, 1034–1043. https://doi.org/10.1093/neuonc/noy027.
Wang, T., Sun, N., Ma, Y., Zhang, S., 2025. Recent advances in the development of Sigma receptor (Radio)ligands and their application in tumors. ACS Pharmacol. Transl. Sci. 8, 951–977. https://doi.org/10.1021/acsptsci.4c00711.
Weller, M., van den Bent, M., Preusser, M., Le Rhun, E., Tonn, J.C., Minniti, G., Bendszus, M., Balana, C., Chinot, O., Dirven, L., French, P., Hegi, M.E., Jakola, A.S., Platten, M., Roth, P., Rudà, R., Short, S., Smits, M., Taphoorn, M.J.B., von Deimling, A., Westphal, M., Soffietti, R., Reifenberger, G., Wick, W., 2021. EANO guidelines on the diagnosis and treatment of diffuse gliomas of adulthood. Nat. Rev. Clin. Oncol. 18, 170–186. https://doi.org/10.1038/s41571-020-00447-z.
Wheeler, K.T., Wang, L.-M., Wallen, C.A., Childers, S.R., Cline, J.M., Keng, P.C., Mach, R. H., 2000. Sigma-2 receptors as a biomarker of proliferation in solid tumours. Br. J. Cancer 82, 1223–1232. https://doi.org/10.1054/bjoc.1999.1067.
Xiong, G., Wu, Z., Yi, J., Fu, L., Yang, Z., Hsieh, C., Yin, M., Zeng, X., Wu, C., Lu, A., Chen, X., Hou, T., Cao, D., 2021. ADMETlab 2.0: an integrated online platform for accurate and comprehensive predictions of ADMET properties. Nucleic Acids Res. 49, W5–W14. https://doi.org/10.1093/nar/gkab255.